Int J Earth Sciences (Geol Rundsch) (2001) 90:623–653
DOI 10.1007/s005310000187

ORIGINAL PAPER

**Wolfgang Müller · Giacomo Prosser
Neil S. Mancktelow · Igor M. Villa · Simon P. Kelley
Giulio Viola · Felix Oberli**

Geochronological constraints on the evolution of the Periadriatic Fault System (Alps)

Received: 9 March 2000 / Accepted: 15 November 2000 / Published online: 24 March 2001

Abstract Fault rocks from various segments of the Periadriatic fault system (PAF; Alps) have been directly dated using texturally controlled Rb–Sr microsampling dating applied to mylonites, and both stepwise-heating and laser-ablation $^{40}Ar/^{39}Ar$ dating applied to pseudotachylytes. The new fault ages place better constraints on tectonic models proposed for the PAF, particularly in its central sector. Along the North Giudicarie fault, Oligocene (E)SE-directed thrusting (29–32 Ma) is currently best explained as accommodation across a cogenetic restraining bend within the Oligocene dextral Tonale-Pustertal fault system. In this case, the limited jump in metamorphic grade observed across the North Giudicarie fault restricts the dextral displacement along the kinematically linked Tonale fault to ~30 km. Dextral displacement between the Tonale and Pustertal faults cannot be transferred via the Peio fault because of both Late Cretaceous fault ages (74–67 Ma) and sinistral transtensive fault kinematics. In combination with other pseudotachylyte ages (62–58 Ma), widespread Late Cretaceous–Paleocene extension is established within the Austroalpine unit, coeval with sedimentation of Gosau Group sediments. Early Miocene pseudotachylyte ages (22–16 Ma) from the Tonale, Pustertal, Jaufen and Passeier faults argue for a period of enhanced fault activity contemporaneous with lateral extrusion of the Eastern Alps. This event coincides with exhumation of the Penninic units and contemporaneous sedimentation within fault-bound basins.

Keywords Dating deformation · Periadriatic fault system · Alps · Mylonites · Pseudotachylytes · Dykes · Rb–Sr microsampling · $^{40}Ar/^{39}Ar$ dating · U–Pb

W. Müller (✉) · N. S. Mancktelow · G. Viola · F. Oberli
Department of Earth Sciences, ETH Zürich, Sonneggstrasse 5, 8092 Zurich, Switzerland
E-mail: wolfgang.mueller@anu.edu.au

G. Prosser
Università della Basilicata, Via Anzio, 85100 Potenza, Italy

Igor M. Villa
Gruppe Isotopengeologie Mineralogisch-Petrographisches Institut, Universität Bern, 3000 Bern, Switzerland

Simon P. Kelley
Department of Earth Sciences, The Open University, Milton Keynes, MK7 6AA, UK

Present address:
W. Müller
Environmental Geochemistry and Geochronology, Research School of Earth Sciences, The Australian National University, Canberra, ACT 0200, Australia

Introduction

The Periadriatic (or Insubric) fault system (PAF) is the most important large-scale fault system of the Alps (e.g. Suess 1885; Argand 1916; Gansser 1968; Laubscher 1988; Schmid et al. 1989; Schmid et al. 1996). The PAF strikes approximately E–W and dissects the entire Alps over a distance of ~700 km from NW Italy to northern Slovenia (Fig. 1). It shows two characteristic bends towards NE strike: the Canavese fault in its westernmost part and the Giudicarie-Mauls fault in its central sector. The PAF separates the Western, Central and Eastern Alps to the north(west) from the Southern Alps (Fig. 1). This division is based mainly on differences in tectonic style, namely large-scale N(W)-vergent thrusting in the north, compared with relatively minor S-vergent thrusting and folding in the south, and the lack of significant Alpine (i.e. Cretaceous and/or Tertiary) metamorphic overprint in the Southern Alps (e.g. Schmid et al. 1989).

The term "Periadriatic fault system" used herein includes both the Periadriatic fault *s. str.*, i.e. the Tonale, Giudicarie-Mauls and Pustertal-Gailtal faults, and several intra-Austroalpine faults located within a few

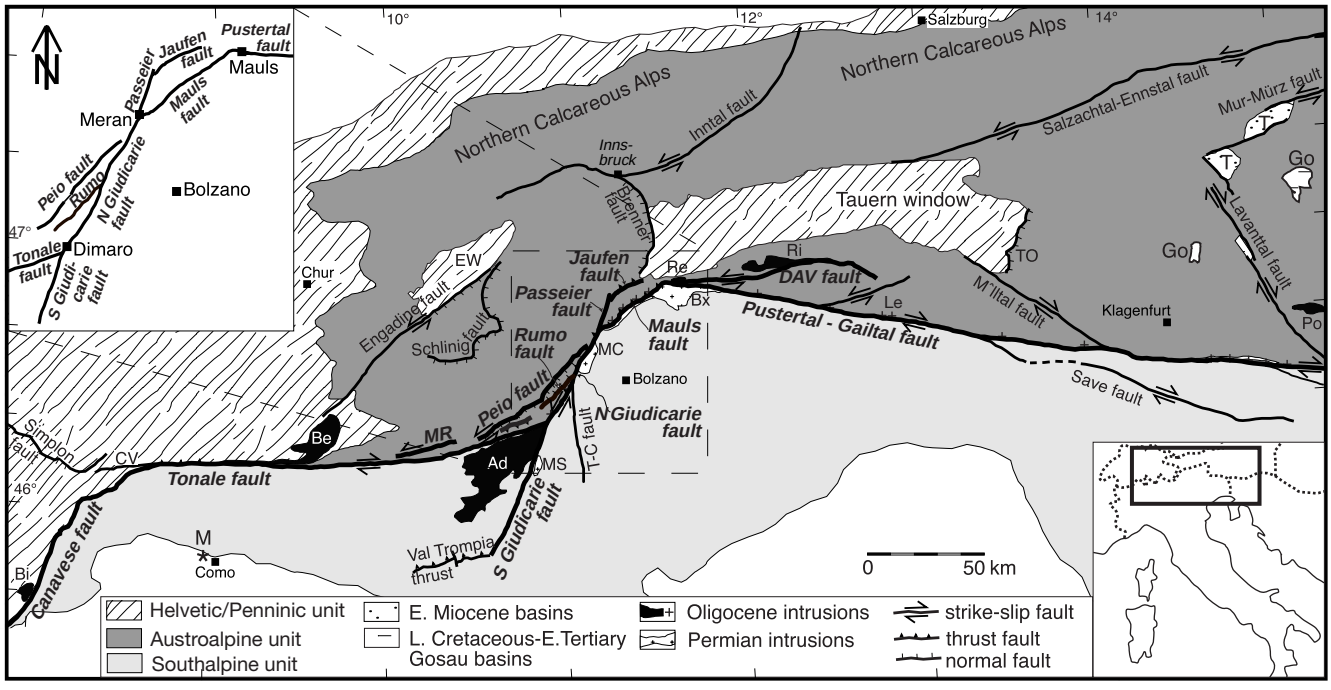

Fig. 1 Simplified tectonic sketch map of the Alps showing all major faults related to the Periadriatic fault system (PAF; *thick black lines*) as well as other faults (*thin black lines*) and major features of the Alps mentioned in the text, based on Bigi et al. (1990) and modified after Neubauer and Genser (1990), Ratschbacher et al. (1991), Mancktelow (1992), Fügenschuh (1995), Grollimund (1996), Froitzheim et al. (1997) and Prosser (1998). The *inset* to the left explains the terminology used for the different parts of the Giudicarie fault in the central sector of the PAF. The Giudicarie fault south of Dimaro is termed South Giudicarie fault (not investigated herein); between Dimaro and Meran it is called North Giudicarie fault and between Meran and Mauls it is called Mauls fault. Faults: *CV* Centovalli; *MR* Mortirollo; *T-C* Trento-Cles; *DAV* Defereggen-Antholz-Vals; *TO* Tauernostrand; plutons: *Bi* Biella; *Be* Bergell; *Ad* Adamello-Presanella; *MS* Monte Sabion; *MC* Monte Croce; *Bx* Brixen; *Re* Rensen; *Ri* Rieserferner; *Le* Lesachtal; *Po* Pohorje; basins: *Go* late Cretaceous–Paleogene "Centralalpine" Gosau Group basins; *T* Miocene basins. *EW* Engadine window; *M* Molasse with Bergell boulders

kilometre-wide zone to the north, namely the Peio, Rumo, Jaufen and Defereggen-Antholz/Anterselva-Vals/Valles (DAV) faults (Fig. 1; Ahrendt 1980; Schmid et al. 1989). The close spatial associations of these intra-Austroalpine faults with the PAF *s. str.* has led to grossly different interpretations of their age and tectonic significance (e.g. Schmid et al. 1989; Martin et al. 1991; Werling 1992). In particular, the tectonic significance of the N(N)E-trending North Giudicarie-Mauls fault and its interaction with the Tonale and Pustertal faults has been interpreted differently for decades, depending also on the role assigned to the Peio fault (Fig. 1; e.g. Werling 1992). Two models have been put forward:

1. During the Neogene, the sinistral North Giudicarie fault deactivated a previously straight dextral Tonale-Pustertal-Gailtal fault that accumulated more than 50 km, and possibly up to 300 km, of displacement (e.g. Laubscher 1971; Ratschbacher et al. 1991; Werling 1992; Schmid et al. 1996; Frisch et al. 1998).
2. The (North) Giudicarie-Mauls fault is, at least in part, a cogenetic part of the Oligocene (or older) PAF *s. str.*, therefore allowing $\leq$50 km (post-)Oligocene dextral displacement along the PAF (Ahrendt 1980; Picotti et al. 1995; Prosser 1998, 2000).

Herein we present new "fault ages" analysed, for the first time, directly from fault rocks using recently developed microsampling techniques to reliably reveal the age(s) of fault activity of the various faults mentioned previously. The aim is to evaluate the (non-)contemporaneity of the different faults and thereby more critically assess the various tectonic models. The techniques applied were Rb–Sr microsampling dating of µg-sized synkinematic mica in mylonites (Müller et al. 2000b) and stepwise-heating and laser-ablation $^{40}Ar/^{39}Ar$ dating of pseudotachylytes (Müller 1998). Ages of fault rocks were independently checked using U–Pb single zircon ages of deformed and undeformed dykes within the fault zones.

Geological setting

The PAF is characterized by different kinematics and tectonic settings from west to east. In the western sector, W of the Bergell/Bregalia pluton (Fig. 1), the PAF is a steeply N-dipping crustal-scale fault zone, characterized by both (back)thrusting and dextral strike-slip (for review see Schmid et al. 1997). Up to

~20 km relative vertical displacement of the northern units has occurred due to backthrusting (Hurford 1986; Heitzmann 1987) during overall dextral transpression (Schmid et al. 1989). By contrast, east of the Bergell pluton, the displacement apparently partitions into a northern, intra-Austroalpine fault system with predominantly sinistral and N-side-up vertical movements, and the Tonale and Pustertal faults, where dextral deformation prevails (e.g. Wiedenbeck 1986; Mancktelow et al., this volume). No major differences in Alpine metamorphic conditions to either side of the eastern Tonale and Pustertal faults are recorded. The jump in Alpine metamorphic conditions occurs along the intra-Austroalpine Peio, Jaufen and DAV faults, which show Alpine higher metamorphic units on their N(W) sides (Fig. 1).

The occurrence of both Permian and Tertiary plutons is the most striking feature of the Periadriatic fault *s. str.* (Fig. 1). The alignment of Permian intrusions has been used to deduce Permian activity along a precursor of the PAF (e.g. Bögel 1975). Oligocene plutons follow the PAF along its whole length (for a review see Exner 1976; von Blanckenburg et al. 1998). Except for the large Bergell, Adamello and Rieserferner intrusives, these Oligocene plutons are thin, elongated and foliated "lamellae" that follow in part the northern rim of the Permian plutons (e.g. Stöckli 1995; Elias 1998). Both their submagmatic to solid-state ductile fabrics and the influence of the contact aureole of the northern Adamello-Presanella intrusion on the mylonites of the Tonale fault constrain an Oligocene, i.e. ~30±2 Ma, age for dextral ductile deformation (e.g. Werling 1992). Abundant cataclasites, discrete faults and pseudotachylytes within these plutons record later, brittle dextral movements along the PAF *s. str.* (e.g. Gansser 1968; Sprenger 1996; Meier 1997).

The amount of accumulated dextral displacement along the PAF *s. str.* is difficult to assess. Estimates that exceed 100 km are based on mostly large-scale palinspastic restorations and/or different Permian–Mesozoic sedimentary facies on both sides of the fault (e.g. Laubscher 1971; Tollmann 1978; Haas et al. 1995; Frisch et al. 1998). Schmid et al. (1989) argue that part of the ~300km dextral displacement suggested by Laubscher (1971) predates the post-late Oligocene movements. Models for the lateral extrusion of the Eastern Alps suggest an eastward increase of the dextral displacement along the Pustertal fault (Neubauer and Genser 1990; Ratschbacher et al. 1991). Based on mainly small-scale mapping, other authors' estimates of the amount of lateral displacement are smaller (Gansser 1968; Ahrendt 1980; Bauer and Schermann 1984; see below).

The major discontinuity in the central sector of the PAF is represented by the N(N)E-trending Giudicarie-Mauls fault, which comprises the Mauls fault and the South and North Giudicarie faults (see inset in Fig. 1 for terminology). A detailed evaluation of the timing and amount of displacement along the North Giudicarie-Mauls fault is a key to any reliable tectonic interpretation of the entire PAF. Along the North Giudicarie fault, top-to-(E)SE thrusting of the Alpine weakly metamorphosed Tonale unit over the Southern Alpine unit takes place along a down-dip, shallowly (W)NW-plunging stretching lineation (Prosser 1998). Thrusting is recorded by low-grade basement- and calcareous mylonites, as well as deformed Oligocene tonalites and their rarely preserved contact aureole (Figs. 2a, b; 3a). Subsequent, middle-late Miocene sinistral transpressive movements are partitioned between WNW-dipping brittle thrusts, and several strike-slip faults within the footwall to the E, e.g. the Trento-Cles-fault. They are kinematically linked to thrusting in the central Southern Alps (Martin et al. 1993; Prosser 1998; Viola 2000); however, Werling (1992) interprets sinistral strike-slip deformation along the North Giudicarie fault to be older than (E)SE-directed thrusting.

The NE-trending Rumo fault is located ~1–2 km W of the North Giudicarie fault. Fault planes dip moderately towards ~NW and sense of shear is towards (W)NW. Kinematics, geometry and the distribution of low-temperature mylonites and pseudotachylytes suggest that the Rumo fault predominantly is a normal fault. Since this sense of shear is opposite to the North Giudicarie fault adjacent to the E, the two faults are not genetically linked (Prosser 1998, 2000).

The NE-trending Peio fault (Fig. 1) separates the Ortler-Campo basement unit to the NW, characterized by Alpine greenschist facies metamorphic conditions, from the Variscan high-grade Tonale unit to the SE, as deduced from the distribution of biotite Rb–Sr ages (Thöni 1981; A. Del Moro, unpublished data). The several-hundred-metres-thick mylonitic belt dips moderately towards SE and shows sinistral transtensive plus N-side-up kinematics related to a shallowly E-plunging stretching lineation (Zarske 1989; Martin et al. 1991; Werling 1992). Pseudotachylytes with similar fault geometries occur along the fault and are considered to be contemporaneous with the mylonites on the basis of mutual overprinting relationships (Fig. 2c, d). The Peio fault mylonites are discordantly cut by acidic dykes (Figs. 2e, 3d; Berger 1989; Werling 1992), which by analogy were considered to be Oligocene in age (e.g. Dal Piaz et al. 1988). Immediately south of the Peio fault, steeply S(SE)-dipping, discrete and thin low-grade shear zones with top-to (W)NW sense of shear occur (Viola 2000). They are characterized by fine-grained, strongly retrogressed mylonitic fabrics (phyllonites) and thin pseudotachylytes. These shear zones were formed during thrusting to the NW, kinematically clearly resolved from that along the Peio fault (*s. str.*) (Martin et al. 1991; Viola 2000).

The Jaufen fault represents the SE border of the Ötztal crystalline basement characterized by Late Cretaceous amphibolite, possibly even eclogite, facies metamorphism (Fig. 1; Del Moro et al. 1982; Hoinkes et al. 1991; Spiess 1995). The Meran-Mauls basement

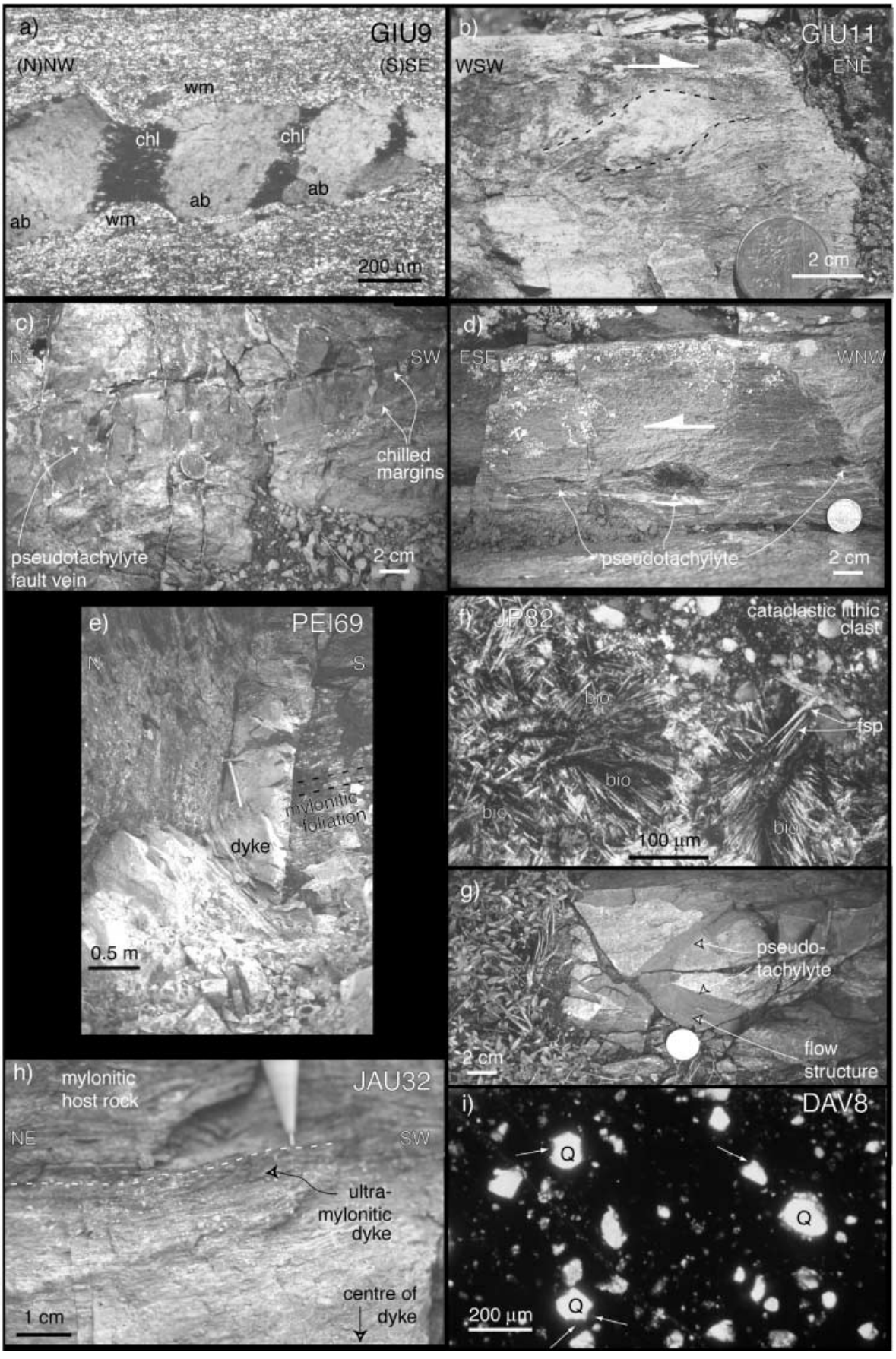
a)
GIU9
(N)NW
(S)SE
wm
chl
chl
ab
ab
ab
wm
200 µm
b)
GIU11
WSW
ENE
2 cm
c)
N
SW
chilled
margins
pseudotachylyte
fault vein
2 cm
d)
ESE
WNW
pseudotachylyte
2 cm
e)
PEI69
N
S
mylonitic
foliation
dyke
0.5 m
f)
JP82
cataclastic lithic
clast
bio
fsp
bio
bio
bio
100 µm
g)
pseudo-
tachylyte
flow
structure
2 cm
h)
mylonitic
host rock
JAU32
NE
SW
ultra-
mylonitic
dyke
centre of
dyke
1 cm
i)
DAV8
Q
Q
Q
200 µm

Fig. 2 Photomicrographs of analysed samples (see Table 1 for location, foliation and lineation). **a** Photomicrograph of thrust-related, low-grade basement mylonite GIU9 from the North Giudicarie fault. Sense of shear is top to (S)SE. Synkinematic chlorite (*chl*) grows between deformationally stretched albite (*ab*), and adjacent newly and/or fully recrystallized white mica (*wm*) is the breakdown product of both plagioclase and large white mica (phyllonite; crossed polarizers; see Fig. 3a). **b** Macroscopic S-type porphyroclast (outlined by *black dashed lines*) indicating thrust-related, top-to-ENE tectonic transport immediately adjacent to sampled calcareous mylonite GIU11 from the N Giudicarie fault (see Fig. 3a). **c** Up to 7 cm-thick pseudotachylyte fault vein from the Peio fault showing characteristic chilled margins (PEI52). **d** Three sinistrally sheared S-type pseudotachylyte porphyroclasts deformed during subsequent mylonitization along the Peio fault (Forcellina di Montozzo). **e** Dyke PEI69 crosscutting the Peio mylonites. The trace of the mylonitic foliation is indicated (see Fig. 3d). **f** Photomicrograph of pseudotachylyte JP82 showing microlitic biotite and rare feldspar fascicles nucleating at tiny clasts. They also show growth into cataclastic lithic clasts resembling amygdales. **g** Anastomosing pattern of Rumo fault pseudotachylytes (RU23, RU24). Macroscopic flow structures are visible within the veins. **h** (Ultra)mylonitic contact between mylonitic host rock (*above dashed line*) and dyke JAU32 (*below dashed line*). The post-intrusive mylonitization is clearly seen. Towards the centre of the dyke (*below*), the intensity of deformations gradually decreases (see Fig. 3c). **i** Photomicrograph of pseudotachylyte DAV8 S of the DAV fault, crossed polarizers. *Arrows* indicate incipient resorption of predominantly quartz clasts by the melt

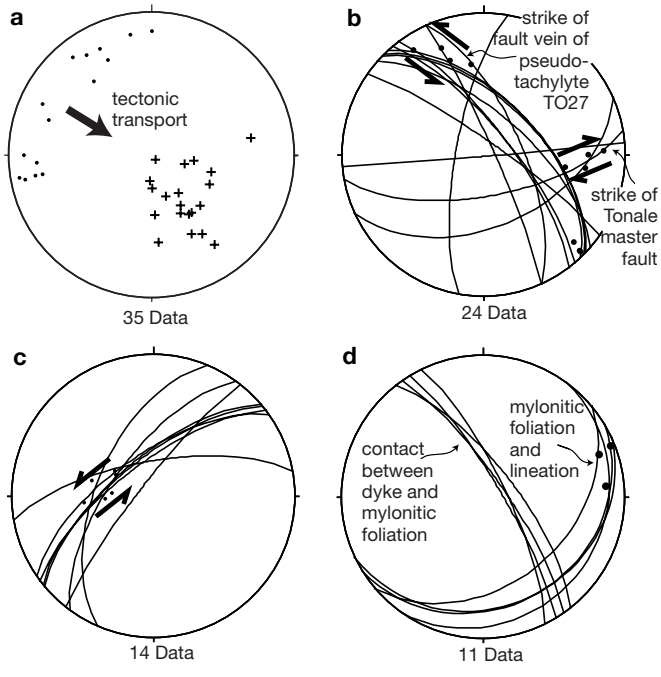

Fig. 3 a–d Stereonets. **a** North Giudicarie fault mylonites (GIU9 and GIU11). **b** Tonale fault related pseudotachylytes (TO27) and associated slickensides plus striations. The fault vein of TO27 represents an antitethic Riedel to the adjacent dextral Tonale fault. **c** Jaufen fault mylonites (JAU32). **d** Peio fault mylonites and crosscutting dyke (PEI69). Equal-area lower-hemisphere projections of lineation (*dots*) and foliation (**b, c, d**: *circles*; **a**: *crosses*, because plotted as poles)

to the SE is weakly overprinted by Alpine metamorphism (Spiess 1995). Two major kinematic events have been recognized along the Jaufen fault by Glutz (1997) and Parolini (1997). Steeply NW-dipping mylonites cut a Late Cretaceous foliation discordantly and bear a moderately W-plunging stretching lineation indicating sinistral plus south-side-up displacement. Syndeformational temperatures have been estimated to be ~300–350 °C (Glutz 1997; Parolini 1997). The observed sense of shear contradicts the overall north-side-up movements deduced from the distribution of mica cooling ages (Del Moro et al. 1982; Spiess 1995). A second, dextral, semiductile to brittle deformation producing mainly cataclasites and pseudotachylytes occurred along steeply dipping fault planes with subhorizontal lineations. It is interpreted to be genetically linked to the deformation along the Mauls fault (Fig. 1).

The NNE-trending Passeier fault (Spiess 1995) in part forms the continuation of the North Giudicarie fault north of Meran and transfers the sinistral strike-slip displacement of the latter northward (Fig. 1; Viola 2000). The fault is characterized by steeply WNW-dipping fault planes marked by protomylonites, ≤30 m-thick blue-black cataclasites and fault gouges as well as rare pseudotachylytes. The Passeier fault cuts off the Jaufen mylonites and displaces the latter to the S(S)W (see Viola 2000 for further discussion).

The approximately E-trending Defereggen-Antholz-Vals (DAV) fault S of the Tauern window represents the southern border of Alpine metamorphism. North of the DAV, Tertiary biotite Rb–Sr ages occur, whereas pre-Alpine ages prevail towards the south (Borsi et al. 1978a). In its present geometry, the DAV-related mylonitic belt is characterized by sinistral strike-slip deformation with a moderate normal fault component (Kleinschrodt 1987; Schulz 1989; Mancktelow et al., this volume). Rare pseudotachylytes occur S of the eastern DAV (Schulz 1989). Several large, Oligocene plutons (Rensen, Zinsnock, Rieserferner) and numerous dykes are present within and in the vicinity of the DAV and provide excellent time markers (Müller et al. 2000b).

This paper addresses the following main problems related to the Periadriatic fault system (Fig. 1):

1. What is the age of ductile, low-grade, top-to-E(SE) thrusting along the North Giudicarie-Mauls fault? Is it possible to establish, on the basis of ages of fault rocks, which model for the evolution of the North Giudicarie fault, and therefore for the whole PAF, is correct?
2. If at least part of the (North) Giudicarie bend was pre-Oligocene, would it be possible to transfer dextral lateral movements from the Tonale into the Pustertal fault via the Peio fault (Laubscher 1970; Schmid et al. 1989)? Critical for this scenario is the age of the Peio fault, which has been proposed to be either Late Cretaceous (Martin et al. 1991; Werling 1992) or Tertiary (Zarske 1989).

3. Are similar kinematics of late movements along the PAF *s. str.* and the northerly adjacent Jaufen fault also reflected in similar ages of related pseudotachylytes? Is deformation associated with lateral extrusion during the Neogene and contemporaneous basin formation reflected also in ages of faults?
4. Do ages of fault zones within the Austroalpine unit reflect a Late Cretaceous extension, as suggested by Fügenschuh (1995) and Froitzheim et al. (1997)?

Results

Results of 11 pseudotachylytes analysed by stepwise-heating and laser-ablation $^{40}Ar/^{39}Ar$ (samples RU23, RU24, T645, PEI74, DAV881b, DAV8, JP82, GI, TO26, JAU13, INS4), two mylonites analysed by Rb–Sr microsampling (GIU9, GIU11) and two dykes analysed by single-zircon U–Pb (PEI69, JAU32) are presented. Details of samples are in Table 1 and Appendix A. Analytical techniques are detailed in Appendix B. The corresponding results are listed in Tables 2, 3, 4 and 5, and are displayed in Figs. 4, 5, 6, 7, 8, 9, 10, 11, 12, 13, 14, 15, 16 and 17. These results are discussed together with geochronological data presented in closely related topical papers (Müller et al. 2000b; Mancktelow et al., this volume; Müller 1998; W. Müller et al., submitted; samples PEI49, PEI52, PEI53, PEI12, PEI26, PEI27, PEI33, BG55, DAV97/2, DAV97/16, JP102, DAV2A, BG169, DAV9, TO27, JAU10, JAU34, PAL35B). All results are presented in four time slices, namely (a) Late Cretaceous–Paleocene, (b) Eocene, (c) Oligocene and (d) Early–Middle Miocene (Figs. 4, 8, 10, 15).

Late Cretaceous–Early Paleocene (75 to ~55 Ma)

The oldest ages (~70 Ma) of fault rocks were obtained from two pseudotachylytes (PEI49, PEI52) and one ultramylonite (PEI53), all collected at the same outcrop of the Peio fault (Fig. 4). Pseudotachylyte PEI49

Table 1 Description and location of the samples for which analytical results are presented herein. The coordinates (right, down) refer to the respective sheets given in parentheses of the Swiss, Italian and Austrian national maps, scale 1:50,000. *Rb–Sr ms* Rb–Sr microsampling dating; *swh Ar–Ar* stepwise-heating $^{40}Ar/^{39}Ar$; *la Ar–Ar* laser-ablation $^{40}Ar/^{39}Ar$; *sz U–Pb* single-zircon U–Pb. For other samples see Müller et al. (2000b), W. Müller et al. (submitted) and Müller (1998)

Sample no. Lithology	Description	Location–description	Location–coordinates	Age (Ma) (Method)
INS4	10 cm-thick fault vein	Outcrop along road (S side) towards Ronco, 650 m SSE Arcegno, Ticino (CH)	700900, 112650; (no. 276, V. Verzasca)	16.4±0.8
Pseudotachylyte	Host rock: high-grade paragneiss composed of albitic plag, qtz, bt showing TiO_2-exsolution lamellae, kfs, subordinate wm and late fractures filled with chl			(swh Ar–Ar)
TO26	~1 cm-thick fault vein with small injection veins that was formed along steeply SSE-dipping fault planes	Road cut along military road towards Forte Presanella (Pozzi Alti), alt. 1620 m; E Passo del Tonale (I)	627200, 5125400 (no. 41, Ponte di Legno)	20.6±5.5
Pseudotachylyte GIU9	Along millimetre- to centimetre-thick layers, intense fluid-enhanced mylonitization and phyllonitization leads to complete replacement of the original medium-grade paragenesis (pl+wm+qtz±bt) by fine-grained (10- to 20-μm) white mica. Plagioclase porphyroclasts show well-developed bookshelf faulting indicating a top-to-ESE sense of shear	Outcrop ~650 m (W)NW Neuhaus/Casanova, N Proveis/Proves (I); small, northern valley along SE slope of Mandelspitz/M. Ometto, alt. 1758 m	655100, 5150650; (no. 26, Appiano/Eppan)	(swh Ar–Ar) 31.6±1.0
Low-grade basement mylonite	Mylonitic foliation 286/36, lineation 334/18			(Rb–Sr ms)
GIU11	Very pure calcareous mylonites with minor quartz, albite and ore minerals. There are no large white mica grains. Calcite grain size varies between ~300 and ~20 μm in thin, foliation-parallel layers	Outcrop ~650 m (W)NW Neuhaus/Casanova, N Proveis/Proves (I); small, northern valley along SE slope of Mandelspitz/M. Ometto, alt. 1755 m	655100, 5150650; (no. 26, Appiano/Eppan)	4–6 μm: 29.8±0.2

Table 1 (continued)

Sample no. Lithology	Description	Location–description	Location–coordinates	Age (Ma) (Method)
Calcareous mylonite	Mylonitic foliation 327/41, lineation 260/23			2–4 μm: 27.5±0.2 <2 μm: 22.9±0.1 (Rb–Sr ms)
GI	Well-preserved pseudotachylyte hosted by a fairly fine-grained amphibolitic paragneiss composed of pl+amph+ep+qtz±chl±kfs	Road cut along forest road 500 m WSW Castello di Altaguardia (2 km SW Rumo); ~5 m above the Giudicarie fault plane	651900, 5132450 (no. 25, Rabbi)	28.9±1.5
Pseudotachylyte				(swh Ar–Ar)
JP82	Black fault vein, 2–3 cm thick, almost no veining into the hosting tonalite	Road cut in Sarntal/Val di Pennes, S Penser Joch/Pso. di Pennes (I), alt. ~1625 m, 600 m WSW Asten/Laste;	233900, 184350 (Austrian map no. 175; Sterzing)	26.9±0.8
Pseudotachylyte	Host rock: Oligocene tonalite (~29–31 Ma; Elias 1998)			(swh Ar–Ar)
RU23	Thick pseudotachylyte veins forming an anastomosing pattern of fault and injection veins	Small creek, alt. 1850 m, 600 m NNW Maso Bernardi, 700 m W M. Alto (2005 m), 3 km (W)NW Rumo (I)	652400, 5147900 (no. 025, Rabbi)	60–57 Ma
Pseudotachylyte	Host rock: strongly retrogressed paragneiss composed of ab, qtz and wm			(la Ar–Ar)
RU24	See RU23	Same as RU23	Same as RU23	~52 Ma (minimum age)
Pseudotachylyte				(swh Ar–Ar)
T645	See Thöni (1981, 1988)	See Thöni (1981, 1988)	See Thöni (1981, 1988)	62±1
Pseudotachylyte				(swh Ar–Ar)
PEI74	~3 cm-thick, black fault vein, which is parallel to the mylonitic foliation. Several, undeformed injection veins that crosscut the mylonitic foliation	Outcrop along path between Rifugio Bozzi and Forcellina di Montozzo, alt. 2510 m, 7 km NE Ponte di Legno (Val di Sole, I)	621200, 5129200 (no. 41, Ponte di Legno)	45.8±0.6
Pseudotachylyte	"Foliation" (pseudotachylyte fault vein): 114/32			(la Ar–Ar)
PEI69	~70 cm-thick dyke with apophyses into, and fuzzy contacts with, the mylonitic host rock. Macroscopic phenocrysts are red grt and white feldspar. Microscopically, the texture is dominated by ab (150 μm) and fine-grained, thin kfs needles (<80 μm); qtz and small wm (~100 μm) form the matrix. No foliation, kfs and wm needles are randomly distributed. Rare, two-phase (up to 5 mm) and fairly abundant smaller (<300 μm) ?mono-phase grt are characteristic minor constituents	Rock wall at Costa di Giogo, (S)E flank of Kirchbergtal, alt. 2265 m, ~300 m W Hint. Alplaner-Alm (Malga Alplaner di dentro), 1.3 km N(N)E Alplanersee/Lago di Alplaner, 3 km S St. Gertraud/Ultental, S. Gertrude/Ultimo, I)	643400, 5146950 (no. 025, Rabbi)	Mean age:
Granitic dyke				~31.9 Ma (ranging between 32.1±0.2 and 31.7±0.1 Ma) (sz U–Pb)

Table 1 (continued)

Sample no. Lithology	Description	Location–description	Location–coordinates	Age (Ma) (Method)
JAU32	Mylonitized dyke, ~1 m thick; magmatic mineralogy: pl+qtz+bt+wm+czo±kfs±grt. Strongly overprinted by subsequent, solid-state (ultra)mylonitization and phyllonitization. Along the margins, magmatic biotite and plagioclase are almost completely replaced by fine-grained (20–40 μm) newly formed white mica. The degree of mylonitization decreases towards the centre of the dyke. Mylonitic foliation 350/20, lineation 294/18.	Road cut along forest road branching off the Jaufenpass/Pso. di M. Giovo road in second bend ENE Walten/Valtina; immediately W of bridge across western creek, alt. 1450 m, 4.2 km (E)NE St. Leonhard in Passeier (S. Leonardo in Passiria, I)	674900, 5189050 (no. 006, S. Leonardo in Passiria/St. Leonhard in Passeier)	31.7±3.4 Ma
Acidic dyke				(sz U–Pb)
JAU13	6 mm-thick injection vein, hosted by a coarse-grained paragneiss (bt–pl–qtz–wm). Thin cataclasites occur along the margins of the pseudotachylyte. The brown matrix contains many rounded clasts composed of quartz and cataclasite, which show different degrees of resorption by the melt. The fine-grained matrix (<5 μm) appears to be slightly recrystallized, but flow structures can still be recognized	Road cut along road towards Vernuer/Vernurio, Gfeis/Gaveis, bend alt. 1103 m, junction towards Vernuer/Vernurio, 6.4 km NNE Meran/Merano (I)	666750, 5177200 (no. 13, Meran/Merano)	17.3±1.1
Pseudotachylyte				(swh Ar–Ar)
DAV 881b	~5 mm-thick, clast-laden fault vein, with small injection veins branching off. At the contact to the host paragneiss (bt+pl+ep+qtz), there is ~2 mm thin cataclastic (precursor?) domain containing angular clasts built up by all paragneiss minerals, including bt. Rounded clasts (<150 μm) occur within the fine-grained, brown, pristine matrix, which show resorption bays indicative for contact with a melt. Clasts: qtz, some feldspar and rare lithic fragments, no bt. Cataclastic rims were avoided during core drilling for step-wise-heating $^{40}Ar/^{39}Ar$ analyses. No signs of alteration or recrystallization	Outcrop along W side of ski track, 350 m (W)NW Brunnalm, alt. 1900 m, 2.5 km SE St. Jakob in Defereggen (A) [collected by B. Schulz]	375350 196300 (178, Hopfgarten in Defereggen)	~60 Ma (?)
Pseudotachylyte				(swh Ar–Ar)
DAV8	Mineralogy of hosting orthogneiss: kfs+wm+bt+pl+qtz	Same as DAV881b	Same as DAV881b	25.5±0.9
Pseudotachylyte	First pseudotachylyte generation: intrudes the host orthogneiss along an anastomosing pattern of injection and fault veins. In thin section, the matrix is nearly transparent and almost isotropic. No details can be resolved optically. Abundant rounded and strongly resorbed clasts (qtz and feldspar) Second pseudotachylyte generation: sharp, black, i.e. very fine-grained, contacts to the first generation, resembling chilled margins. Towards the centre of the injection vein (from where the analysed drill cores were taken), the matrix becomes slightly coarser grained. Very many rounded and resorbed clasts (qtz and feldspar). No recrystallization phenomena "Foliation" (pseudotachylyte fault vein): 180/35			(swh Ar–Ar)

Table 2 Rb–Sr isotopic data (errors are 95% c.l.)

Sample	Rb (ppm)	Sr (ppm)	$^{87}Rb/^{86}Sr$	$^{87}Sr/^{86}Sr$	Age (Ma)	$(^{87}Sr/^{86}Sr)_i$
GIU9 wm1	432	53.2	23.580	0.735095±190	31.6±1.0	0.724512±281
GIU9 chl1	2.62	10.3	0.7463	0.724847±272		
GIU11 leach	–	–	0.0005	0.710668±13		
GIU11<2 μm	276	28.4	28.207	0.719832±21	22.88±0.13	0.710668±13
GIU11 2–4 μm	272	25.3	31.183	0.722824±26	27.45±0.15	0.710668±13
GIU11 4–6 μm	285	26.6	31.069	0.723794±13	29.75±0.15	0.710668±13

yielded a stepwise-heating $^{40}Ar/^{39}Ar$ age of 74±2 Ma (82% ^{39}Ar released), which is virtually identical to the Rb–Sr microsampling 8-point errorchron age of ultramylonite PEI53 indicating 72.2±9.8 Ma (Müller 1998; W. Müller et al., submitted). The second pseudotachylyte PEI52 yielded a slightly more complex apparent age spectrum. Five pristine melt-related steps yielded an age of 67±3 Ma (54% ^{39}Ar released), which is similar to the other two fault ages from the same outcrop (W. Müller et al., submitted). This suggests concomitant Late Cretaceous formation of mylonites and pseudotachylytes, which is consistent with field observations (Fig. 2c, d; see above).

Slightly younger, but internally consistent, ages (62–~58 Ma) are recorded by three extension-related pseudotachylytes collected from different faults; these include samples from S of the DAV fault (DAV881b), from the Rumo fault (RU23, RU24) and from the base of the Silvretta nappe (T645; Fig. 4; e.g. Froitzheim et al. 1997). The latter is not related to the PAF but was chosen for a methodological comparison because of existing K–Ar and Rb–Sr data (Thöni 1981, 1988).

Two Rumo fault pseudotachylytes analysed by either laser-ablation (RU23) or stepwise-heating analysis (RU24) indicate Paleocene ages. Fifteen individual laser-spot analyses of pseudotachylyte RU23 are characterized by similar $^{39}Ar/^{40}Ar$ and very low $^{36}Ar/^{40}Ar$ ratios forming a tight cluster when plotted on the inverse isochron plot. A weighted mean apparent age of 57.3±1.4 Ma can be calculated (Fig. 5a). The individual spot analyses exhibit a weak negative correlation between age and Cl/K ratio, interpreted as signs of incipient alteration; hence, ages of ~60 Ma from lowest Cl/K-spots are taken as the best approximation for the formation of pseudotachylyte RU23. Pseudotachylyte RU24 records a staircase age spectrum over virtually all ^{39}Ar released with apparent ages ranging between 6 and 114 Ma. High Ca/K and Cl/K ratios of the first five steps (~10% ^{39}Ar) and, less pronounced, also for steps 6 and 7, reveal the presence of distinct young alteration phases (Fig. 5b). Older ages at highest release temperatures are attributed to inherited clasts, as suggested by high Ca/K and Cl/K ratios. The age–Cl/K diagram shows mixing trends towards alteration phases for steps 1–7 and mixing trends towards clasts for steps 12–16 (Fig. 5c). The inferred pristine melt composition is located at the intersection of these mixing lines, approximated best by steps 8–11 (~65% ^{39}Ar), which show very similar Ca/K (~0.04) and Cl/K ratios (~0.0015). Because corresponding ages for least altered steps 8–11 regularly increase from 49 to 54 Ma, these ages must be regarded as minimum age for formation of RU24.

The stepwise-heating $^{40}Ar/^{39}Ar$ analysis of pseudotachylyte DAV881b yielded apparent ages ranging between 22 and 130 Ma, but a fairly flat spectrum indicating ~60 Ma for 80% ^{39}Ar released (Fig. 6a). Since ~80% ^{39}Ar is released at temperatures >1000 °C, where phyllosilicates, in particular biotite, have

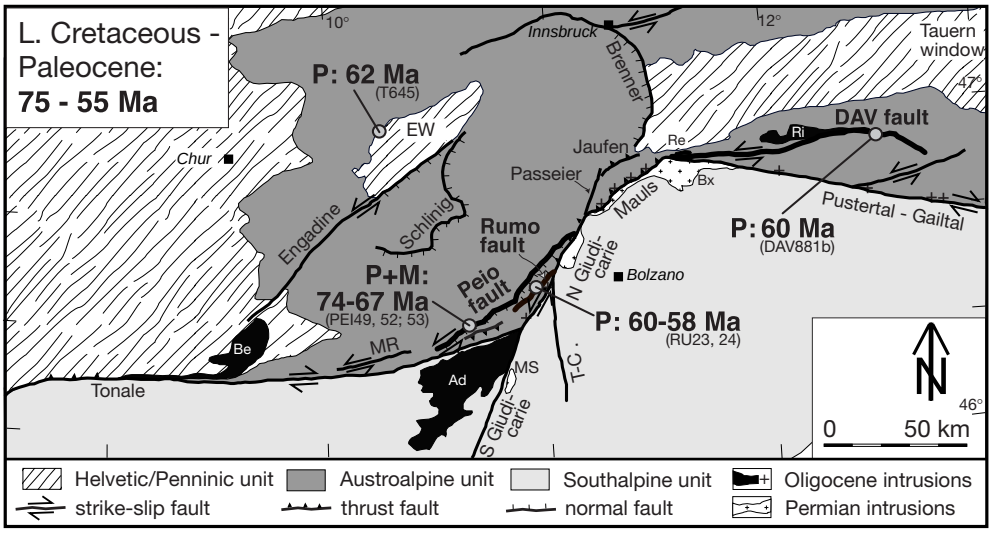

Fig. 4 Simplified tectonic sketch map of the central sector of the PAF. Locations and ages of Late Cretaceous–Paleocene fault rocks are indicated. *P* Pseudotachylyte stepwise-heating and/or laser ablation $^{40}Ar/^{39}Ar$ age; *M* mylonite Rb–Sr microsampling age. For additional abbreviations see Fig. 1

Table 3 $^{40}Ar/^{39}Ar$ stepwise-heating isotopic data (errors are 1σ)

DAV 881b Step no.	Temp (°C)	^{40}Ar (pl/g)	^{39}Ar (pl/g)	% ^{39}Ar	^{38}Ar (pl/g)	^{37}Ar (pl/g)	^{36}Ar (pl/g)	Age (Ma)	$^{39}Ar/^{40}Ar$	$^{36}Ar/^{40}Ar$
Step 1	591	3268.193±0.953	9.672±0.010	0.82	2.829±0.006	4.369±0.067	10.980±0.039	22.13±11.00	2.96e-03±3.30e-06	3.36e-03±1.20e-05
Step 2	666	648.688±0.572	12.191±0.015	1.03	1.206±0.004	5.672±0.057	2.010±0.010	40.33±2.20	1.88e-02±2.70e-05	3.10e-03±1.50e-05
Step 3	725	232.372±0.200	15.642±0.020	1.33	1.283±0.005	6.099±0.047	0.606±0.004	30.86±0.70	6.73e-02±9.60e-05	2.61e-03±1.70e-05
Step 4	782	264.835±0.167	22.148±0.029	1.88	2.127±0.004	7.755±0.057	0.574±0.003	38.68±0.33	8.36e-02±1.10e-04	2.17e-03±9.90e-06
Step 5	833	826.884±0.448	38.373±0.037	3.25	4.629±0.010	13.244±0.071	2.079±0.010	49.76±0.65	4.64e-02±5.10e-05	2.51e-03±1.10e-05
Step 6	882	617.180±0.334	32.513±0.036	2.76	5.139±0.010	10.571±0.034	1.257±0.008	67.50±0.60	5.27e-02±6.40e-05	2.04e-03±1.20e-05
Step 7	930	718.884±0.381	35.698±0.037	3.03	6.297±0.012	12.579±0.100	1.396±0.005	76.40±0.38	4.97e-02±5.60e-05	1.94e-03±7.10e-06
Step 8	975	1120.337±0.229	45.756±0.046	3.88	8.371±0.015	18.289±0.057	2.534±0.010	72.43±0.58	4.08e-02±4.20e-05	2.26e-03±9.10e-06
Step 9	1016	3059.604±1.048	102.438±0.095	8.68	18.541±0.033	43.374±0.129	7.940±0.029	62.38±0.72	3.35e-02±3.30e-05	2.60e-03±9.30e-06
Step 10	1056	3231.982±0.167	120.802±0.105	10.24	20.335±0.036	50.876±0.143	8.161±0.029	60.87±0.62	3.74e-02±3.30e-05	2.53e-03±8.90e-06
Step 11	1093	2239.425±0.067	100.832±0.091	8.54	16.476±0.029	41.426±0.114	5.199±0.019	62.45±0.48	4.50e-02±3.90e-05	2.32e-03±8.30e-06
Step 12	1145	1465.517±0.200	79.041±0.071	6.70	12.878±0.023	32.026±0.100	3.117±0.011	61.71±0.38	5.39e-02±4.80e-05	2.13e-03±7.70e-06
Step 13	1195	1651.299±0.152	106.844±0.095	9.05	15.068±0.027	39.744±0.114	3.189±0.011	59.46±0.28	6.47e-02±5.70e-05	1.93e-03±6.90e-06
Step 14	1248	2721.167±0.219	172.648±0.152	14.63	23.055±0.041	65.061±0.172	5.470±0.020	57.40±0.30	6.34e-02±5.60e-05	2.01e-03±7.20e-06
Step 15	1350	4707.678±0.905	256.170±0.224	21.71	32.414±0.057	112.657±0.305	10.257±0.036	58.74±0.37	5.44e-02±4.90e-05	2.18e-03±7.70e-06
Step 16	1408	348.380±0.081	14.494±0.014	1.23	2.112±0.006	14.174±0.062	0.617±0.004	101.56±0.67	4.16e-02±4.00e-05	1.77e-03±1.10e-05
Step 17	1559	407.331±0.086	14.814±0.014	1.26	2.172±0.005	18.018±0.067	0.630±0.003	131.36±0.56	3.64e-02±3.40e-05	1.55e-03±7.80e-06
j=5.03e-03			K=3.35%		Cl=972 ppm	Ca=2.59%		t(K/Ar)=60.8		Weight 0.07135 g

RU24 Step no.	Temp (°C)	^{40}Ar (pl/g)	^{39}Ar (pl/g)	% ^{39}Ar	^{38}Ar (pl/g)	^{37}Ar (pl/g)	^{36}Ar (pl/g)	Age (Ma)	$^{39}Ar/^{40}Ar$	$^{36}Ar/^{40}Ar$
Step 1	520	124.930±0.039	1.320±0.003	0.92	0.106±0.002	0.046±0.014	0.397±0.002	6.36±0.41	1.06e-02±2.10e-05	3.18e-03±1.30e-05
Step 2	591	35.955±0.021	1.794±0.004	1.25	0.068±0.002	0.286±0.015	0.094±0.002	5.06±0.35	4.99e-02±1.20e-04	2.61e-03±5.40e-05
Step 3	648	30.697±0.036	2.186±0.002	1.52	0.061±0.001	0.201±0.014	0.054±0.001	7.37±0.17	7.12e-02±1.20e-04	1.77e-03±3.80e-05
Step 4	715	55.979±0.028	3.099±0.004	2.16	0.117±0.002	0.253±0.020	0.052±0.002	14.37±0.20	5.54e-02±8.20e-05	9.35e-04±3.40e-05
Step 5	779	124.742±0.080	4.394±0.004	3.06	0.129±0.000	0.203±0.012	0.077±0.003	25.48±0.19	3.52e-02±4.20e-05	6.13e-04±2.00e-05
Step 6	834	432.757±0.682	12.130±0.023	8.45	0.312±0.002	0.468±0.005	0.208±0.004	33.48±0.13	2.80e-02±6.90e-05	4.81e-04±8.70e-06
Step 7	873	779.124±1.275	18.301±0.036	12.75	0.418±0.002	0.662±0.013	0.299±0.003	41.20±0.11	2.35e-02±6.00e-05	3.84e-04±3.60e-06
Step 8	912	935.878±1.394	19.260±0.033	13.42	0.397±0.002	0.476±0.005	0.212±0.002	49.38±0.11	2.06e-02±4.60e-05	2.26e-04±1.70e-06
Step 9	952	1028.599±1.097	21.410±0.036	14.91	0.488±0.003	0.533±0.033	0.164±0.004	49.85±0.11	2.08e-02±4.00e-05	1.59e-04±3.40e-06
Step 10	990	1473.974±0.890	30.066±0.030	20.94	0.519±0.004	0.513±0.015	0.165±0.003	51.59±0.07	2.04e-02±2.40e-05	1.12e-04±1.90e-06
Step 11	1030	1074.802±0.593	20.556±0.024	14.32	0.360±0.002	0.439±0.012	0.160±0.001	54.36±0.07	1.91e-02±2.50e-05	1.49e-04±1.10e-06
Step 12	1077	376.274±0.187	6.365±0.006	4.43	0.159±0.005	0.332±0.020	0.097±0.001	59.32±0.09	1.69e-02±1.70e-05	2.57e-04±3.90e-06
Step 13	1122	126.397±0.053	1.703±0.003	1.19	0.148±0.002	0.373±0.017	0.132±0.002	55.85±0.32	1.35e-02±2.60e-05	1.04e-03±1.30e-05
Step 14	1205	66.814±0.030	0.544±0.002	0.38	0.102±0.001	0.088±0.003	0.110±0.001	68.57±0.81	8.15e-03±3.30e-05	1.64e-03±2.00e-05
Step 15	1336	55.057±0.023	0.299±0.001	0.21	0.058±0.003	0.185±0.024	0.079±0.005	113.73±5.20	5.44e-03±2.30e-05	1.43e-03±9.20e-05
Step 16	1536	51.695±0.023	0.135±0.002	0.09	0.046±0.002	0.164±0.009	0.070±0.001	236.97±4.30	2.61e-03±3.90e-05	1.36e-03±2.50e-05
j=0.000612			K=3.35%		Cl=73 ppm	Ca=0.22%		t(K/Ar)=46.1		Weight 0.11466 g

T645 Step no.	Temp (°C)	^{40}Ar (pl/g)	^{39}Ar (pl/g)	% ^{39}Ar	^{38}Ar (pl/g)	^{37}Ar (pl/g)	^{36}Ar (pl/g)	Age (Ma)	$^{39}Ar/^{40}Ar$	$^{36}Ar/^{40}Ar$
Step 1	524	53.003±0.048	0.356±0.002	0.32	0.047±0.003	0.010±0.005	0.168±0.002	6.73±1.60	6.72e-03±2.60e-05	3.17e-03±3.50e-05
Step 2	610	20.886±0.133	0.720±0.002	0.63	0.032±0.003	0.053±0.008	0.045±0.002	8.13±0.57	3.45e-02±8.10e-05	2.15e-03±4.70e-05
Step 3	650	25.052±0.058	0.910±0.004	0.80	0.038±0.002	0.047±0.003	0.022±0.001	16.00±0.40	3.63e-02±9.70e-05	8.92e-04±3.60e-05
Step 4	706	70.816±0.194	1.864±0.003	1.62	0.037±0.002	0.107±0.003	0.062±0.003	22.59±0.39	2.63e-02±6.10e-05	8.80e-04±3.40e-05
Step 5	766	138.802±0.269	3.460±0.006	2.99	0.077±0.001	0.231±0.005	0.045±0.002	29.30±0.13	2.49e-02±5.40e-05	3.23e-04±1.00e-05
Step 6	803	131.914±0.102	1.966±0.004	1.70	0.052±0.001	0.116±0.004	0.036±0.004	49.37±0.52	1.49e-02±2.80e-05	2.73e-04±2.90e-05

Step 7	841	194.001±0.170	2.630±0.003	2.27	0.082±0.001	0.148±0.006	0.042±0.003	55.37±0.28	1.36e-02±1.90e-05	2.14e-04±1.40e-05
Step 8	889	469.918±0.409	6.458±0.008	5.57	0.128±0.004	0.272±0.005	0.060±0.003	56.32±0.15	1.37e-02±2.10e-05	1.27e-04±7.20e-06
Step 9	935	631.560±0.443	8.262±0.010	7.12	0.150±0.002	0.385±0.008	0.054±0.002	59.90±0.10	1.31e-02±1.80e-05	8.50e-05±2.80e-06
Step 10	980	929.557±0.545	12.034±0.013	10.37	0.219±0.002	0.536±0.003	0.076±0.002	60.62±0.08	1.29e-02±1.60e-05	8.15e-05±1.90e-06
Step 11	1022	815.697±0.102	10.174±0.010	8.77	0.197±0.002	0.528±0.002	0.084±0.002	62.48±0.07	1.25e-02±1.20e-05	1.02e-04±2.30e-06
Step 12	1060	786.923±0.029	9.843±0.009	8.48	0.176±0.003	0.590±0.006	0.056±0.002	62.88±0.07	1.25e-02±1.10e-05	7.18e-05±2.40e-06
Step 13	1117	881.462±0.024	10.861±0.010	9.36	0.210±0.003	0.716±0.004	0.084±0.002	63.37±0.07	1.23e-02±1.10e-05	9.54e-05±1.90e-06
Step 14	1183	1244.283±0.051	15.617±0.014	13.45	0.287±0.002	0.948±0.005	0.080±0.002	62.84±0.07	1.26e-02±1.10e-05	6.45e-05±1.80e-06
Step 15	1260	1885.066±0.681	24.003±0.022	20.67	0.418±0.002	1.433±0.011	0.101±0.002	62.18±0.06	1.27e-02±1.30e-05	5.35e-05±8.20e-07
Step 16	1330	364.634±0.273	4.434±0.005	3.83	0.105±0.002	0.259±0.010	0.052±0.002	63.21±0.12	1.22e-02±1.50e-05	1.42e-04±4.60e-06
Step 17	1445	186.508±0.167	2.155±0.003	1.86	0.059±0.002	0.162±0.013	0.038±0.003	65.00±0.34	1.16e-02±1.80e-05	2.06e-04±1.50e-05
Step 18	1545	30.231±0.041	0.198±0.003	0.18	0.031±0.002	0.021±0.009	0.044±0.003	66.08±3.20	6.56e-03±6.70e-05	1.45e-03±6.60e-05
j=4.54e-04			K=3.66%		Cl=42 ppm	Ca=0.38%		t(K/Ar)=59.0	(Thöni 1981: 59±3 Ma)	Weight 0.09979 g

GI Step no.	Temp (°C)	^{40}Ar (pl/g)	^{39}Ar (pl/g)	% ^{39}Ar	^{38}Ar (pl/g)	^{37}Ar (pl/g)	^{36}Ar (pl/g)	Age (Ma)	^{39}Ar/^{40}Ar	^{36}Ar/^{40}Ar
Step 1	289	76.520±0.019	2.348±0.003	0.66	0.249±0.003	3.633±0.012	0.209±0.002	75.10±3.60	3.07e-02±3.30e-05	2.74e-03±3.00e-05
Step 2	447	35.940±0.009	4.620±0.005	1.29	0.207±0.004	8.294±0.023	0.060±0.002	48.96±1.60	1.29e-01±1.20e-04	1.66e-03±5.10e-05
Step 3	519	38.495±0.029	10.764±0.010	3.01	0.573±0.004	15.451±0.042	0.055±0.003	26.08±0.87	2.80e-01±2.70e-04	1.43e-03±5.90e-05
Step 4	584	63.943±0.023	15.364±0.014	4.29	1.077±0.003	15.909±0.042	0.087±0.004	30.66±0.91	2.40e-01±2.10e-04	1.37e-03±5.60e-05
Step 5	615	12.464±0.010	4.624±0.005	1.29	0.354±0.003	3.929±0.011	0.004±0.002	30.31±1.20	3.71e-01±3.00e-04	2.87e-04±8.20e-05
Step 6	658	112.729±0.029	29.206±0.027	8.16	2.019±0.005	24.414±0.065	0.122±0.002	32.24±0.26	2.59e-01±2.30e-04	1.08e-03±1.80e-05
Step 7	700	50.864±0.014	14.316±0.014	4.00	0.957±0.003	12.283±0.033	0.049±0.002	31.14±0.52	2.82e-01±2.40e-04	9.71e-04±3.70e-05
Step 8	738	57.971±0.006	17.198±0.016	4.81	1.173±0.003	18.476±0.050	0.047±0.002	31.67±0.41	2.97e-01±2.40e-04	8.13e-04±3.20e-05
Step 9	780	59.410±0.010	18.987±0.017	5.31	1.480±0.003	22.873±0.062	0.040±0.002	31.10±0.33	3.20e-01±2.60e-04	6.77e-04±2.60e-05
Step 10	811	59.977±0.014	20.212±0.018	5.65	1.730±0.004	28.397±0.073	0.034±0.003	30.92±0.40	3.37e-01±2.80e-04	5.64e-04±3.50e-05
Step 11	857	125.867±0.020	39.163±0.035	10.94	5.414±0.010	98.060±0.258	0.065±0.002	34.88±0.15	3.11e-01±2.70e-04	5.20e-04±1.20e-05
Step 12	890	106.767±0.012	30.988±0.027	8.66	7.880±0.015	118.051±0.311	0.054±0.002	38.60±0.12	2.90e-01±2.40e-04	5.03e-04±8.70e-06
Step 13	934	72.204±0.007	18.345±0.017	5.13	4.380±0.008	71.419±0.189	0.041±0.001	42.79±0.21	2.54e-01±2.20e-04	5.64e-04±1.40e-05
Step 14	984	65.088±0.008	13.876±0.012	3.88	2.114±0.005	45.961±0.123	0.051±0.002	46.07±0.43	2.13e-01±1.80e-04	7.84e-04±2.40e-05
Step 15	1052	56.908±0.042	8.723±0.008	2.44	0.949±0.004	35.969±0.096	0.045±0.002	63.24±0.54	1.53e-01±1.60e-04	7.89e-04±2.20e-05
Step 16	1169	483.451±0.051	85.709±0.076	23.94	11.488±0.020	334.989±0.885	0.227±0.003	61.37±0.10	1.77e-01±1.60e-04	4.70e-04±3.80e-06
Step 17	1356	608.739±0.113	22.268±0.020	6.22	3.696±0.008	116.398±0.308	0.222±0.002	277.98±0.31	3.66e-02±3.40e-05	3.65e-04±2.20e-06
Step 18	1445	82.977±0.018	1.174±0.002	0.33	0.275±0.004	6.279±0.017	0.086±0.003	516.23±6.80	1.41e-02±2.20e-05	1.04e-03±3.40e-05
j=6.7e-03			K=0.76%		Cl=225 ppm	Ca=3.83%		t(K/Ar)=58.8		Weight 0.08840 g

JP82 Step no.	Temp (°C)	^{40}Ar (pl/g)	^{39}Ar (pl/g)	% ^{39}Ar	^{38}Ar (pl/g)	^{37}Ar (pl/g)	^{36}Ar (pl/g)	Age (Ma)	^{39}Ar/^{40}Ar	^{36}Ar/^{40}Ar
Step 1	568	124.377±0.019	7.959±0.007	4.79	0.352±0.002	1.284±0.018	0.152±0.001	10.97±0.04	6.40e-02±5.90e-05	1.22e-03±6.60e-06
Step 2	637	133.217±0.045	5.677±0.006	3.42	0.298±0.003	1.054±0.012	0.042±0.002	23.32±0.11	4.26e-02±4.40e-05	3.13e-04±1.30e-05
Step 3	701	248.528±0.178	8.740±0.010	5.26	0.502±0.002	1.387±0.014	0.072±0.002	28.47±0.09	3.52e-02±4.70e-05	2.88e-04±8.40e-06
Step 4	758	234.408±0.084	7.698±0.008	4.63	0.519±0.002	1.510±0.014	0.083±0.002	29.84±0.10	3.28e-02±3.70e-05	3.53e-04±9.00e-06
Step 5	810	163.668±0.101	5.433±0.007	3.27	0.387±0.003	1.501±0.018	0.086±0.001	27.83±0.08	3.32e-02±4.80e-05	5.27e-04±7.10e-06
Step 6	860	163.479±0.091	5.500±0.006	3.31	0.333±0.002	1.844±0.015	0.088±0.002	27.33±0.10	3.36e-02±4.20e-05	5.41e-04±9.30e-06
Step 7	908	135.722±0.055	4.408±0.005	2.65	0.298±0.003	1.465±0.015	0.090±0.002	27.04±0.15	3.25e-02±3.80e-05	6.66e-04±1.40e-05
Step 8	952	173.947±0.091	5.628±0.006	3.39	0.393±0.002	2.092±0.014	0.112±0.002	27.41±0.12	3.24e-02±4.00e-05	6.42e-04±1.10e-05
Step 9	995	327.065±0.097	10.934±0.010	6.58	0.732±0.003	4.728±0.022	0.150±0.002	28.34±0.07	3.34e-02±3.20e-05	4.58e-04±6.50e-06
Step 10	1035	321.876±0.078	11.211±0.011	6.74	0.788±0.002	4.273±0.019	0.128±0.001	27.77±0.05	3.48e-02±3.40e-05	3.97e-04±3.80e-06
Step 11	1076	268.668±0.062	9.737±0.009	5.86	0.711±0.003	3.241±0.028	0.104±0.002	26.76±0.07	3.62e-02±3.40e-05	3.88e-04±6.60e-06
Step 12	1113	253.276±0.058	9.262±0.008	5.57	0.700±0.002	3.459±0.017	0.121±0.002	25.73±0.06	3.66e-02±3.40e-05	4.79e-04±5.90e-06
Step 13	1164	329.821±0.049	12.193±0.011	7.33	0.950±0.003	5.110±0.028	0.129±0.002	26.23±0.06	3.70e-02±3.40e-05	3.92e-04±5.60e-06

Table 3 (continued)

JP82 Step no.	Temp (°C)	^{40}Ar (pl/g)	^{39}Ar (pl/g)	% ^{39}Ar	^{38}Ar (pl/g)	^{37}Ar (pl/g)	^{36}Ar (pl/g)	Age (Ma)	^{39}Ar/^{40}Ar	^{36}Ar/^{40}Ar
Step 14	1230	832.681±0.182	31.061±0.028	18.68	1.997±0.004	13.380±0.039	0.258±0.003	26.72±0.04	3.73e-02±3.40e-05	3.10e-04±3.20e-06
Step 15	1310	840.599±0.097	26.850±0.024	16.14	1.679±0.003	14.483±0.045	0.302±0.002	30.67±0.04	3.19e-02±2.80e-05	3.59e-04±2.30e-06
Step 16	1386	105.017±0.023	1.950±0.003	1.18	0.145±0.002	1.215±0.024	0.122±0.003	38.50±0.43	1.86e-02±2.70e-05	1.16e-03±2.30e-05
Step 17	1537	162.250±0.039	1.988±0.004	1.20	0.187±0.003	1.803±0.010	0.204±0.002	55.58±0.33	1.23e-02±2.50e-05	1.26e-03±1.20e-05
j=6.12e-04			K=3.88%		Cl=458 ppm	Ca=2.74%		t(K/Ar)=27.4		Weight 0.10485 g

DAV8 Step no.	Temp (°C)	^{40}Ar (pl/g)	^{39}Ar (pl/g)	% ^{39}Ar	^{38}Ar (pl/g)	^{37}Ar (pl/g)	^{36}Ar (pl/g)	Age (Ma)	^{39}Ar/^{40}Ar	^{36}Ar/^{40}Ar
Step 1	560	629.993±0.159	4.875±0.006	1.75	0.438±0.003	0.304±0.025	1.901±0.007	15.37±0.47	7.74e-03±1.00e-05	3.02e-03±1.10e-05
Step 2	633	163.144±0.015	6.714±0.006	2.42	0.146±0.003	0.442±0.031	0.204±0.003	16.82±0.12	4.12e-02±3.70e-05	1.25e-03±1.50e-05
Step 3	698	220.939±0.043	8.359±0.008	3.01	0.232±0.005	0.577±0.037	0.191±0.002	21.55±0.08	3.78e-02±3.40e-05	8.65e-04±8.80e-06
Step 4	757	188.326±0.096	5.507±0.007	1.98	0.206±0.003	0.498±0.011	0.201±0.002	25.59±0.13	2.92e-02±3.80e-05	1.07e-03±1.10e-05
Step 5	810	453.260±0.064	12.316±0.011	4.43	0.412±0.003	0.684±0.021	0.527±0.004	26.46±0.11	2.72e-02±2.50e-05	1.16e-03±9.30e-06
Step 6	860	376.337±0.055	11.417±0.011	4.11	0.370±0.003	0.660±0.023	0.289±0.002	27.89±0.07	3.03e-02±2.90e-05	7.67e-04±5.50e-06
Step 7	907	254.781±0.025	7.794±0.007	2.80	0.282±0.003	0.522±0.023	0.182±0.003	28.21±0.14	3.06e-02±2.80e-05	7.13e-04±1.30e-05
Step 8	951	479.107±0.027	15.234±0.015	5.48	0.532±0.003	0.738±0.018	0.341±0.003	27.18±0.06	3.18e-02±2.90e-05	7.13e-04±5.20e-06
Step 9	995	642.306±0.141	20.988±0.020	7.54	0.588±0.002	0.904±0.023	0.534±0.003	25.29±0.05	3.27e-02±3.10e-05	8.32e-04±4.50e-06
Step 10	1036	723.643±0.096	22.502±0.020	8.09	0.645±0.003	1.194±0.030	0.596±0.003	26.65±0.05	3.11e-02±2.80e-05	8.24e-04±4.30e-06
Step 11	1075	701.482±0.077	22.663±0.021	8.15	0.626±0.003	1.433±0.022	0.539±0.003	26.21±0.05	3.23e-02±3.00e-05	7.68e-04±3.80e-06
Step 12	1121	588.823±0.073	19.561±0.018	7.03	0.523±0.003	1.426±0.025	0.471±0.003	25.18±0.06	3.32e-02±3.00e-05	8.00e-04±5.20e-06
Step 13	1172	568.307±0.031	18.931±0.017	6.80	0.453±0.003	1.648±0.013	0.461±0.003	25.00±0.05	3.33e-02±3.00e-05	8.12e-04±4.90e-06
Step 14	1230	1353.199±0.109	43.401±0.039	15.60	1.061±0.003	3.310±0.022	1.348±0.005	24.12±0.05	3.21e-02±2.90e-05	9.96e-04±4.10e-06
Step 15	1305	1590.839±0.096	47.970±0.043	17.24	1.220±0.004	5.164±0.023	1.542±0.006	25.94±0.05	3.02e-02±2.70e-05	9.70e-04±3.80e-06
Step 16	1390	282.200±0.037	4.001±0.005	1.44	0.215±0.002	1.849±0.034	0.204±0.002	60.12±0.19	1.42e-02±1.90e-05	7.22e-04±7.50e-06
Step 17	1565	412.735±0.159	5.956±0.006	2.14	0.280±0.003	0.782±0.029	0.343±0.003	56.70±0.16	1.44e-02±1.60e-05	8.32e-04±6.40e-06
j=6.12e-04			K=6.50%		Cl=162 ppm	Ca=0.95%		t(K/Ar)=26.4		Weight 0.07464 g

INS4 Step no.	Temp (°C)	^{40}Ar (pl/g)	^{39}Ar (pl/g)	% ^{39}Ar	^{38}Ar (pl/g)	^{37}Ar (pl/g)	^{36}Ar (pl/g)	Age (Ma)	^{39}Ar/^{40}Ar	^{36}Ar/^{40}Ar
Step 1	724	8.459±0.540	0.185±0.006	0.71	0.051±0.003	0.441±0.011	0.001±0.002	38.57±2.50	2.19e-02±7.50e-05	9.44e-05±3.00e-05
Step 2	822	124.368±0.329	1.752±0.007	5.85	0.148±0.005	3.434±0.030	0.354±0.002	11.24±0.36	1.41e-02±4.00e-05	2.85e-03±1.20e-05
Step 3	875	220.770±2.014	3.906±0.021	12.90	0.220±0.004	6.697±0.020	0.517±0.010	17.38±0.76	1.77e-02±1.20e-04	2.34e-03±3.80e-05
Step 4	923	170.416±1.031	4.158±0.004	13.73	0.162±0.004	7.425±0.031	0.367±0.003	14.97±0.20	2.44e-02±7.30e-05	2.15e-03±1.50e-05
Step 5	966	126.206±0.118	4.380±0.006	14.45	0.147±0.003	6.623±0.032	0.176±0.002	16.93±0.16	3.47e-02±3.30e-05	1.40e-03±1.20e-05
Step 6	1013	81.245±0.034	3.707±0.004	12.25	0.115±0.002	3.928±0.016	0.047±0.003	18.10±0.24	4.56e-02±2.90e-05	5.78e-04±1.90e-05
Step 7	1070	106.772±0.079	5.017±0.005	16.53	0.120±0.002	6.329±0.024	0.083±0.002	16.39±0.13	4.70e-02±3.10e-05	7.78e-04±1.20e-05
Step 8	1202	89.671±0.041	4.610±0.006	15.20	0.121±0.002	10.938±0.030	0.052±0.002	16.19±0.11	5.14e-02±3.60e-05	5.83e-04±1.10e-05
Step 9	1350	59.850±0.034	1.866±0.004	6.21	0.082±0.003	9.594±0.028	0.035±0.003	26.56±0.43	3.12e-02±3.00e-05	5.79e-04±2.10e-05
Step 10	1500	39.997±0.026	0.510±0.003	1.78	0.075±0.003	3.165±0.017	0.055±0.002	43.95±1.30	1.27e-02±2.80e-05	1.38e-03±2.10e-05
j=5.56e-04			K=0.78%		Cl=8 ppm	Ca=2.79%		t(K/Ar)=17.5		Weight 0.06922 g

TO26 Step no.	Temp (°C)	^{40}Ar (pl/g)	^{39}Ar (pl/g)	% ^{39}Ar	^{38}Ar (pl/g)	^{37}Ar (pl/g)	^{36}Ar (pl/g)	Age (Ma)	^{39}Ar/^{40}Ar	^{36}Ar/^{40}Ar
Step 1	570	638.298±0.179	19.669±0.018	12.95	1.241±0.003	2.482±0.021	1.133±0.005	16.96±0.09	3.08e-02±2.80e-05	1.77e-03±7.90e-06
Step 2	637	496.466±0.104	16.186±0.015	10.66	1.038±0.003	1.378±0.022	0.151±0.002	30.55±0.05	3.26e-02±3.10e-05	3.04e-04±4.20e-06
Step 3	700	724.524±0.257	22.974±0.022	15.13	1.393±0.004	1.414±0.017	0.119±0.001	32.82±0.04	3.17e-02±3.10e-05	1.64e-04±1.80e-06
Step 4	758	630.200±0.089	20.356±0.019	13.41	1.119±0.003	1.074±0.013	0.085±0.002	32.51±0.04	3.23e-02±3.00e-05	1.35e-04±3.10e-06
Step 5	811	327.721±0.075	10.811±0.010	7.12	0.575±0.003	0.799±0.020	0.051±0.001	31.61±0.05	3.30e-02±3.20e-05	1.56e-04±4.00e-06
Step 6	860	158.500±0.033	4.686±0.005	3.09	0.266±0.003	0.301±0.031	0.034±0.002	34.54±0.12	2.96e-02±2.90e-05	2.16e-04±9.70e-06
Step 7	908	140.335±0.029	3.893±0.005	2.57	0.222±0.003	0.311±0.019	0.026±0.002	37.09±0.13	2.77e-02±3.30e-05	1.88e-04±1.00e-05
Step 8	975	193.785±0.032	5.185±0.005	3.42	0.303±0.002	0.427±0.011	0.049±0.002	37.67±0.13	2.68e-02±2.80e-05	2.55e-04±1.00e-05
Step 9	1040	419.908±0.035	10.141±0.009	6.68	0.604±0.003	0.675±0.018	0.095±0.002	42.12±0.07	2.42e-02±2.20e-05	2.26e-04±4.30e-06
Step 10	1098	384.617±0.043	8.565±0.008	5.64	0.511±0.004	0.649±0.011	0.094±0.002	45.40±0.09	2.23e-02±2.00e-05	2.43e-04±5.60e-06
Step 11	1150	419.682±0.068	8.684±0.009	5.72	0.526±0.002	0.862±0.022	0.116±0.002	48.29±0.08	2.07e-02±2.10e-05	2.77e-04±4.20e-06
Step 12	1215	618.656±0.071	11.329±0.011	7.47	0.670±0.002	1.563±0.017	0.200±0.002	53.69±0.07	1.83e-02±1.70e-05	3.22e-04±2.60e-06
Step 13	1318	720.881±0.100	8.452±0.009	5.57	0.522±0.003	1.266±0.015	0.254±0.002	82.39±0.11	1.17e-02±1.20e-05	3.52e-04±2.80e-06
Step 14	1546	919.545±0.086	0.845±0.004	0.56	0.284±0.003	0.310±0.014	0.301±0.003	843.82±3.00	9.19e-04±4.00e-06	3.27e-04±3.20e-06
j=6.12e-04			K=3.55%		Cl=371 ppm	Ca=0.58%		t(K/Ar)=43.0		Weight 0.09518 g

JAU13 Step no.	Temp (°C)	^{40}Ar (pl/g)	^{39}Ar (pl/g)	% ^{39}Ar	^{38}Ar (pl/g)	^{37}Ar (pl/g)	^{36}Ar (pl/g)	Age (Ma)	^{39}Ar/^{40}Ar	^{36}Ar/^{40}Ar
Step 1	530	239.978±1.197	14.659±0.058	15.58	0.269±0.001	0.402±0.023	0.290±0.003	9.25±0.08	6.11e-02±3.70e-04	1.21e-03±1.50e-05
Step 2	610	75.156±2.395	4.085±0.050	4.34	0.064±0.004	0.111±0.009	0.000±0.003	16.09±0.54	5.44e-02±1.60e-03	3.32e-06±3.70e-05
Step 3	665	128.073±2.453	5.570±0.041	5.92	0.086±0.003	0.177±0.020	0.011±0.004	19.61±0.43	4.35e-02±8.20e-04	8.68e-05±3.30e-05
Step 4	711	222.103±2.073	9.289±0.041	9.87	0.168±0.004	0.300±0.009	0.040±0.005	19.82±0.24	4.18e-02±4.10e-04	1.81e-04±2.10e-05
Step 5	767	297.366±0.905	12.750±0.027	13.55	0.208±0.003	0.345±0.011	0.057±0.005	19.27±0.13	4.29e-02±1.50e-04	1.93e-04±1.80e-05
Step 6	818	256.054±0.876	11.351±0.025	12.06	0.195±0.002	0.315±0.019	0.052±0.002	18.57±0.09	4.43e-02±1.70e-04	2.04e-04±8.10e-06
Step 7	874	191.377±0.350	9.173±0.009	9.75	0.168±0.002	0.256±0.012	0.063±0.002	16.49±0.07	4.79e-02±9.60e-05	3.31e-04±1.00e-05
Step 8	920	108.470±0.321	5.357±0.009	5.69	0.119±0.002	0.198±0.003	0.043±0.002	15.67±0.10	4.94e-02±1.50e-04	3.95e-04±1.60e-05
Step 9	961	131.081±0.274	5.751±0.006	6.11	0.133±0.002	0.214±0.008	0.068±0.001	16.89±0.07	4.39e-02±9.70e-05	5.22e-04±9.40e-06
Step 10	1004	70.311±0.047	2.521±0.003	2.68	0.049±0.001	0.121±0.013	0.053±0.002	18.95±0.17	3.59e-02±4.00e-05	7.52e-04±2.20e-05
Step 11	1064	117.852±0.038	3.693±0.004	3.93	0.095±0.002	0.107±0.013	0.074±0.002	22.71±0.13	3.13e-02±3.10e-05	6.27e-04±1.50e-05
Step 12	1118	193.015±0.041	4.418±0.005	4.70	0.109±0.003	0.206±0.011	0.113±0.002	31.51±0.13	2.29e-02±2.30e-05	5.85e-04±1.10e-05
Step 13	1186	241.106±0.096	4.106±0.004	4.37	0.111±0.002	0.307±0.006	0.128±0.001	43.04±0.09	1.70e-02±1.90e-05	5.30e-04±4.60e-06
Step 14	1266	143.260±0.053	0.969±0.002	1.04	0.047±0.002	0.201±0.016	0.086±0.002	103.27±0.54	6.77e-03±1.40e-05	6.00e-04±1.30e-05
Step 15	1552	315.545±0.055	0.374±0.003	0.40	0.062±0.002	0.208±0.011	0.205±0.002	510.31±3.2	1.19e-03±8.20e-06	6.49e-04±5.50e-06
j=4.88e-04			K=2.75%		Cl=32 ppm	Ca=0.19%		t(K/Ar)=21.7		Weight 0.11643 g

Table 4 $^{40}Ar/^{39}Ar$ isotope data and apparent ages of laser-spot analyses (errors are 1σ)

RU23 j=0.003105	^{40}Ar (fl)	^{39}Ar (fl)	^{38}Ar (fl)	^{37}Ar (fl)	^{36}Ar (fl)	Age (Ma)	$^{39}Ar/^{40}Ar$	$^{36}Ar/^{40}Ar$
1 Dark matrix	165.661±1.382	15.752±0.294	0.292±0.013	1.111±0.064	0.018±0.005	56.09±1.26	9.51e-02±1.94e-03	1.12e-04±2.85e-05
2 Dark matrix	82.855±0.954	7.552±0.105	0.108±0.013	0.027±0.111	0.010±0.005	58.24±1.48	9.12e-02±1.65e-03	1.25e-04±5.71e-05
3 Dark matrix	73.418±0.584	6.646±0.109	0.094±0.013	0.063±0.115	0.004±0.009	59.84±2.34	9.05e-02±1.65e-03	5.70e-05±1.16e-04
4 Dark matrix	64.312±0.857	5.783±0.071	0.089±0.009	0.233±0.097	–0.004±0.004	62.43±1.69	8.99e-02±1.63e-03	–6.62e-05±6.95e-05
5 Dark matrix	183.127±1.411	17.004±0.206	0.273±0.013	0.800±0.134	0.008±0.004	58.57±0.97	9.29e-02±1.33e-03	4.48e-05±2.44e-05
6 Dark matrix	53.468±0.265	4.833±0.059	0.128±0.013	0.328±0.080	0.004±0.004	59.57±1.70	9.04e-02±1.19e-03	7.70e-05±8.36e-05
7 Dark matrix	97.251±1.247	9.278±0.239	0.158±0.013	0.782±0.134	0.004±0.004	57.09±1.82	9.54e-02±2.75e-03	4.11e-05±4.60e-05
8 Dark matrix	88.141±0.588	8.502±0.118	0.149±0.009	0.328±0.062	0.025±0.004	52.42±1.20	9.65e-02±1.48e-03	2.85e-04±5.08e-05
9 Dark matrix	67.331±0.672	6.430±0.109	0.115±0.009	0.044±0.080	0.004±0.009	56.68±2.42	9.55e-02±1.88e-03	6.22e-05±1.27e-04
10 Dark matrix	97.681±0.403	9.408±0.109	0.162±0.009	0.196±0.116	0.004±0.004	56.53±1.06	9.63e-02±1.19e-03	4.25e-05±4.58e-05
11 Dark, near clasts	95.521±0.588	9.020±0.126	0.149±0.009	0.385±0.080	0.013±0.009	56.15±1.76	9.44e-02±1.44e-03	1.31e-04±8.94e-05
12 Small clasts	74.700±0.445	7.207±0.122	0.158±0.004	0.405±0.080	0.012±0.004	54.36±1.41	9.65e-02±1.73e-03	1.67e-04±5.99e-05
13 Dark matrix	153.204±2.533	14.241±0.294	0.286±0.017	1.263±0.135	0.012±0.004	57.90±1.63	9.30e-02±2.46e-03	8.01e-05±2.92e-05
14 Small clasts	15.210±0.194	1.475±0.029	0.042±0.004	0.025±0.080	0.004±0.009	52.28±9.39	9.70e-02±2.30e-03	2.76e-04±5.61e-04
15 Dark matrix	83.411±0.664	7.164±0.063	0.132±0.009	0.425±0.098	0.017±0.004	60.35±1.27	8.59e-02±1.02e-03	2.00e-04±5.36e-05
PEI74 j=0.003102	^{40}Ar (fl)	^{39}Ar (fl)	^{38}Ar (fl)	^{37}Ar (fl)	^{36}Ar (fl)	Age (Ma)	$^{39}Ar/^{40}Ar$	$^{36}Ar/^{40}Ar$
1 Dark matrix	226.123±3.406	26.974±0.407	0.364±0.013	1.269±0.111	0.023±0.005	44.96±1.03	1.193e-01±2.545e-03	1.001e-04±2.096e-05
2 Dark matrix	183.722±1.466	20.845±0.298	0.283±0.013	0.902±0.111	0.023±0.005	46.91±0.88	1.135e-01±1.859e-03	1.237e-04±2.575e-05
3 Dark matrix	262.927±2.634	30.981±0.512	0.420±0.013	1.536±0.092	0.019±0.004	45.90±0.94	1.178e-01±2.278e-03	7.177e-05±1.706e-05
4 Dark matrix	224.836±1.684	25.845±0.323	0.331±0.013	0.946±0.126	0.023±0.004	46.59±0.77	1.150e-01±1.676e-03	1.033e-04±1.994e-05
5 Dark matrix	338.642±1.844	38.055±0.546	0.536±0.021	2.424±0.126	0.056±0.009	46.74±0.83	1.124e-01±1.725e-03	1.667e-04±2.525e-05
6 Dark matrix	456.281±2.701	56.053±0.508	0.720±0.025	2.764±0.075	0.023±0.009	44.33±0.58	1.228e-01±1.330e-03	4.988e-05±1.873e-05
7 Clast	128.832±1.231	16.735±0.227	0.245±0.017	0.328±0.092	0.019±0.004	40.72±0.83	1.299e-01±2.154e-03	1.489e-04±3.481e-05
8 Dark matrix	166.162±2.550	19.411±0.349	0.249±0.017	0.937±0.109	0.019±0.009	45.70±1.31	1.168e-01±2.759e-03	1.145e-04±5.145e-05
9 Dark matrix	237.257±2.524	28.701±0.517	0.371±0.017	1.014±0.111	0.008±0.004	45.22±0.99	1.210e-01±2.529e-03	3.431e-05±1.875e-05
10 Clast	336.944±5.040	31.377±0.634	0.452±0.009	1.689±0.111	0.211±0.009	48.34±1.39	9.312e-02±2.342e-03	6.250e-04±2.698e-05
11 Small clasts	320.819±3.751	33.966±0.596	0.482±0.013	2.126±0.147	0.114±0.009	46.70±1.11	1.059e-01±2.233e-03	3.550e-04±2.690e-05
12 Dark matrix	140.728±0.866	16.832±0.151	0.225±0.009	0.891±0.111	–0.003±0.009	46.52±0.98	1.196e-01±1.302e-03	–2.422e-05±6.059e-05
13 Dark matrix	96.057±0.505	11.222±0.118	0.140±0.009	0.618±0.094	0.005±0.009	46.55±1.36	1.168e-01±1.370e-03	5.268e-05±8.876e-05
14 Dark matrix	173.418±0.635	21.191±0.172	0.285±0.013	1.383±0.129	0.001±0.009	45.17±0.79	1.222e-01±1.089e-03	3.837e-06±4.917e-05
15 Dark matrix	237.524±1.647	28.054±0.223	0.371±0.013	1.621±0.094	0.022±0.009	45.53±0.72	1.181e-01±1.244e-03	9.096e-05±3.590e-05

Table 5 Single zircon U–Pb isotopic data from dykes PEI69 and JAU32

Sample description[a]	Weight (µg)	U (ppm)	Pb_{rad} (pg)	Pb_{comm}[b] (pg)	$^{206}Pb/^{204}Pb$[c]	$^{207}Pb/^{206}Pb$[d]	$^{208}Pb/^{206}Pb$[d]	$^{207}Pb/^{235}U$[d]	$^{206}Pb/^{238}U$[d,e]	ρ[f]	$^{207}Pb/^{235}U$ age (Ma)	$^{206}Pb/^{238}U$ age[e] (Ma)	$^{232}Th/^{238}U$
PEI69													
Z1 (L_5)	1.9	1105	9.55	3.5	202.8	0.04561±182	0.01762±563	0.03130±135	0.004993±23	0.756	31.289±1.329	32.106±0.145	0.054
Z3 (S_6–S_7)	1.1	1249	6.36	3.2	147.5	0.04599±252	0.04492±768	0.03129±185	0.004950±28	0.819	31.280±1.826	31.830±0.180	0.137
Z4 (S_{16})	1.6	863	7.58	1.3	330.2	0.04679±110	0.2514±29	0.03170±80	0.004927±16	0.628	31.688±0.789	31.681±0.101	0.764
JAU32													
Z1 (L_5)	3.0	1606	21.5	4.4	341.5	0.04721±109	0.01180±326	0.03194±80	0.004908±13	0.725	31.926±0.786	31.665±0.084	0.036
Z3 (L_2)	11.3	965	97.3	3.3	1758	0.05074±85	0.1554±21	0.06016±112	0.008598±52	0.465	59.319±1.077	55.283±0.336	0.472
Z4 (–)	2.9	470	18.8	4.9	250.0	0.05453±111	0.1224±33	0.1024±23	0.01362±6	0.611	99.011±2.143	87.315±0.368	0.372
Z5 (L_5)	4.5	1523	30.8	2.6	809.9	0.04693±47	0.01240±132	0.03192±35	0.004934±10	0.579	31.908±0.345	31.834±0.061	0.038
Z6 (L_2)	5.2	403	33.7	3.8	542.1	0.05530±71	0.1519±20	0.1181±17	0.01549±4	0.631	113.32±1.52	99.151±0.235	0.462

[a] Morphological classification after Pupin (1980)
[b] Total common Pb including analytical blank and tracer contribution
[c] Measured value corrected for SEM mass discrimination and fractionation
[d] Data corrected for SEM mass discrimination and fractionation, tracer contribution, laboratory blank and 32 Ma sample common Pb contribution (Cumming and Richards 1975; model III)
[e] $^{206}Pb/^{238}U$-ratios and $^{206}Pb/^{238}U$-ages corrected by $1e^{-05}$ to $2e^{-05}$ (or +80 to 90 ka), respectively, for initial disequilibrium in $^{230}Th/^{238}U$, adopting Th/U=3 for the crystallization environment
[f] Correlation coefficient of radiogenic $^{207}Pb/^{235}U$ vs $^{206}Pb/^{238}U$
Uncertainties are given at the 95% c.l. level and refer to the least significant digits

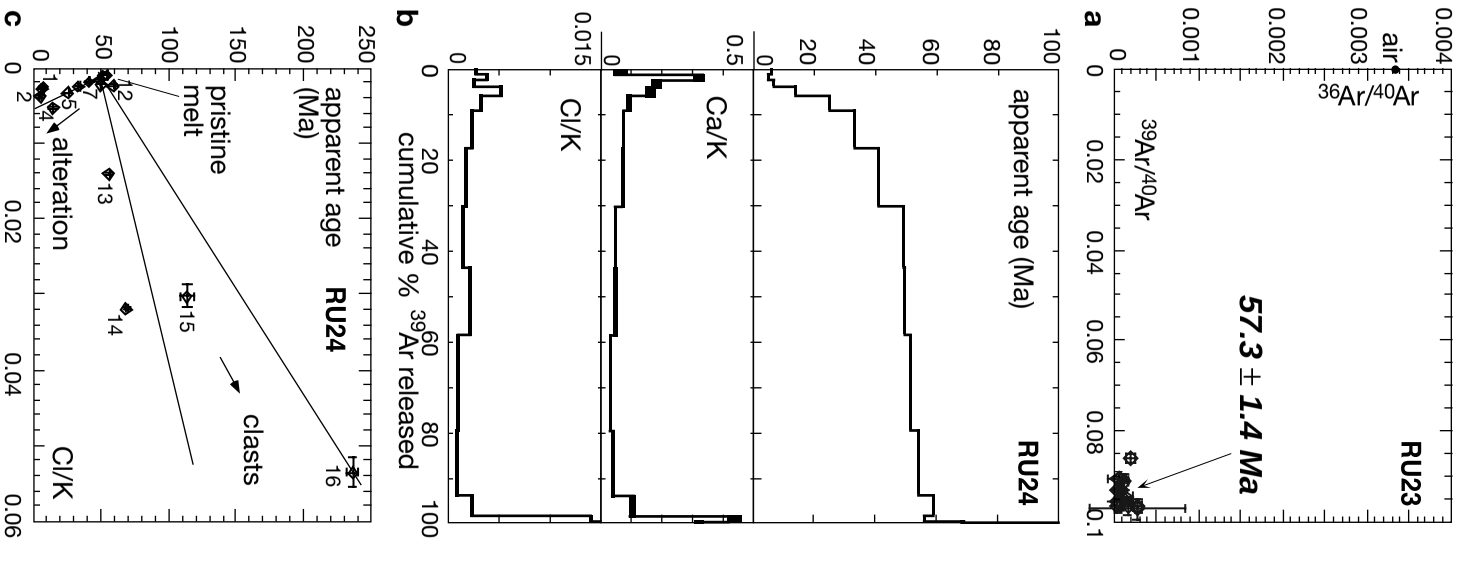

Fig. 5 $^{40}Ar/^{39}Ar$ isochron diagram of **a** laser-ablation, and **b, c** stepwise-heating analyses of pseudotachylytes RU23 and RU24

released most of their Ar due to in-vacuo breakdown (Lo et al. 2000), a feldspar-rich matrix composition is inferred. The K concentration of 3.35% points to a matrix composed of both plagioclase and K-feldspar. The trajectories in chemical discrimination diagrams based on Ar isotopes (Fig. 6b) are complex and do

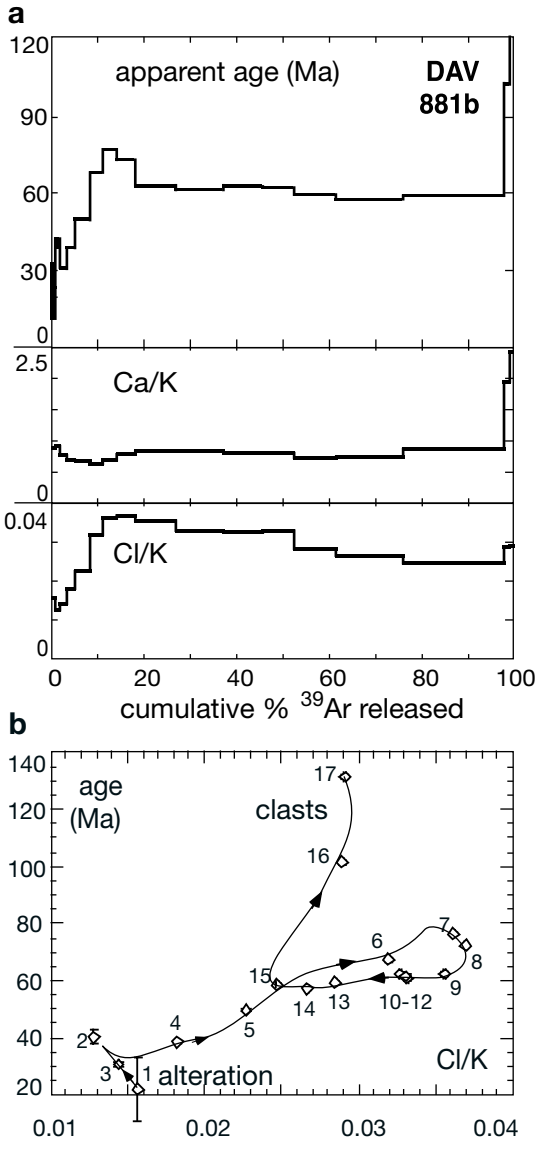

Fig. 6 **a** $^{40}Ar/^{39}Ar$ stepwise-heating spectra and **b** corresponding mineral chemical discrimination diagram based on Ar isotopes for pseudotachylyte DAV881b

not allow an unequivocal interpretation of the age spectrum. Rather uniform Ca/K ratios (except for clast-related high Ca/K steps 16 and 17) contrast with variable Cl/K ratios, whose positive correlation with apparent ages may suggest the presence of inherited ^{40}Ar. Elevated $^{36}Ar/^{39}Ar$ ratios and young apparent ages of steps 1–3 are indicative of later alteration. High Cl/K ratios and old apparent ages of steps 7–9 may argue for Ar release from a mineral phase contaminated by inherited/excess ^{40}Ar, such as biotite or fluid inclusions in the matrix (Turner and Wang 1992; Müller 1998). Steps 10–15 release >70% ^{39}Ar and show slightly decreasing Cl/K ratios but similar apparent ages between 62 and 57 Ma. If regressed in an isochron diagram, these steps yield an age of 55.8± 5.3 Ma and an atmospheric trapped $^{40}Ar/^{36}Ar$ ratio of 306±15. The age of ~60 Ma may also represent a "pseudoplateau" reflecting the admixture of inherited ^{40}Ar as indicated by elevated Cl/K ratios, which would mask a possibly younger age (see DAV8). Since this is considered to be unlikely, a Paleocene age (~60 Ma) – in agreement with similar ages within the Austroalpine unit – is interpreted to be most probable.

Pseudotachylyte T645 was analysed by stepwise-heating $^{40}Ar/^{39}Ar$ in order to complement and evaluate existing K/Ar and Rb–Sr data (Thöni 1981, 1988). It shows a discordant age spectrum with ages ranging from 7 to 66 Ma. Ages are older than 60 Ma over ~85% ^{39}Ar released (Fig. 7). The corresponding Ca/K and Cl/K ratios reveal little variation indicating a fairly homogeneous melt. Weak positive correlation between ages and Ca/K ratios indicates some inheritance, which – given that the oldest age is only 66 Ma – appears to be very small. Similarly, a weak negative correlation between age and Cl/K ratio is interpreted as signs of incipient alteration. Strong alteration is visible for steps 1–8. Based on chemical discrimination, a mean age of 62±1 Ma is calculated (~80% ^{39}Ar released). The calculated total-gas age (59 Ma) and the K concentration (3.66%) are identical to K/Ar data by Thöni (1981; 58±3 Ma; 3.66%); however, the corresponding Rb–Sr age of 78.5±4.6 Ma is older (Thöni 1988). Incomplete digestion and/or homogenization of Sr-bearing feldspars and heterogeneity in initial $^{87}Sr/^{86}Sr$ ratios of the precursor rock may be responsible for the observed shift towards older Rb–Sr ages.

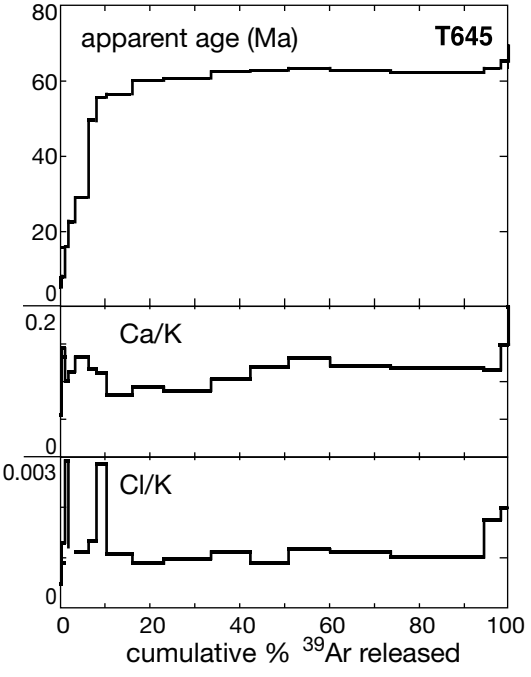

Fig. 7 $^{40}Ar/^{39}Ar$ stepwise-heating spectra of pseudotachylyte T645

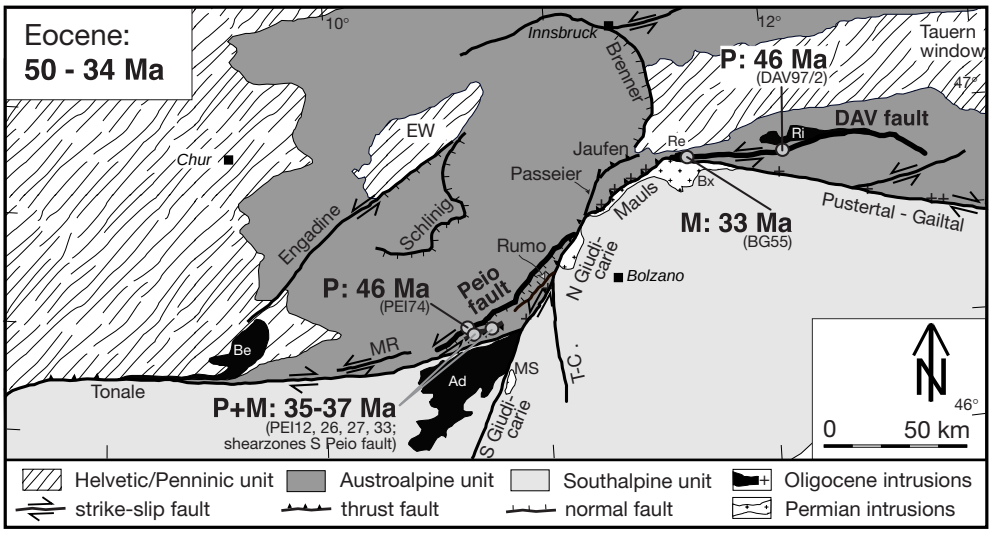

Fig. 8 Simplified tectonic sketch map of the central sector of the PAF. Locations and ages of Eocene fault rocks are indicated. See Figs. 1 and 4 for abbreviations

Eocene (~50–34 Ma)

Fifteen individual laser-ablation $^{40}Ar/^{39}Ar$ analyses were performed on pseudotachylyte PEI74 from the Peio fault. When plotted on an isochron diagram, 12 analyses form a tight cluster with low $^{36}Ar/^{40}Ar$ ratios (Figs. 8, 9). Their mean apparent age is 45.8±0.6 Ma, which is identical within error to the age of 45.1± 0.9 Ma obtained from an isochron regression. Due to the limited range in $^{39}Ar/^{40}Ar$, the resulting trapped $^{40}Ar/^{36}Ar$ of 449±155 is imprecise. Analyses 7, 10 and 11 contain inherited (10, 11) or altered (7) minerals, as indicated by both petrographic observations prior to analysis and resulting elevated Ca/K and Cl/K ratios. Pseudotachylyte PEI74 suggests renewed Early Eocene activity along the Peio fault.

Two pseudotachylytes (PEI12, PEI26) and two mylonites (PEI27, PEI33) were sampled along thin, discrete shear zones immediately S of the Peio fault (Fig. 8). Their top-to-(W)NW tectonic transport is clearly different from the adjacent Peio fault (see Viola 2000). Both stepwise-heating and laser-ablation $^{40}Ar/^{39}Ar$ dating (pseudotachylytes) and Rb–Sr microsampling analyses (mylonites) yielded similar ages between 35 and 37 Ma, suggesting Late Eocene thrusting within the Tonale unit south of the Peio fault (Viola 2000; W. Müller et al., submitted).

Mylonites and both foliation parallel and crosscutting pseudotachylytes occur immediately south of the Zinsnock intrusion (S of Rieserferner pluton; Mancktelow et al., this volume; Fig. 8). This mylonite zone is clearly crosscut by the Oligocene Zinsnock intrusion. A foliation parallel pseudotachylyte (DAV97/2) yielded a stepwise-heating $^{40}Ar/^{39}Ar$ age of 46±3 Ma (Mancktelow et al., this volume). Along the western DAV fault, a mylonite (BG55) recording sinistral strike-slip deformation was sampled (BG55; Fig. 8). Fine-grained white mica domains grown between stretched K-feldspar were dated by Rb–Sr microsampling, yielding an age of 33.4±1.3 Ma (see Müller et al. 2000b; Mancktelow et al., this volume).

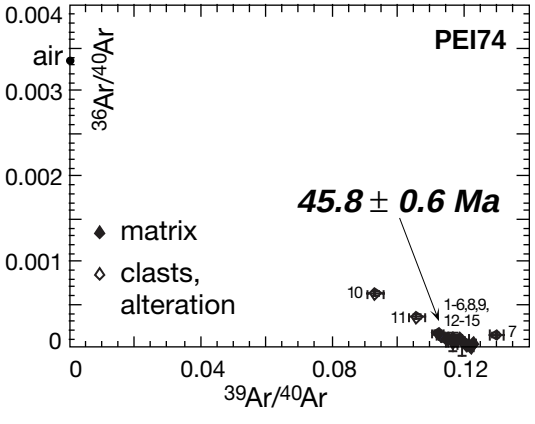

Fig. 9 $^{40}Ar/^{39}Ar$ isochron diagram of laser-ablation analyses of pseudotachylyte PEI74

Oligocene (32–25 Ma)

During the Early Oligocene (32–30 Ma), intense magmatic activity is recorded along the whole PAF and adjacent tectonic units (for a review see Berger et al. 1996; von Blanckenburg et al. 1998; Fig. 10). The degree of deformation of the plutons, their contact aureoles and dykes provides key time constraints for the evolution of the PAF. Several dykes related to this Periadriatic magmatism within the Peio (PEI69), Jaufen (JAU32) and DAV (BG169, DAV2A, JP102A; Müller et al. 2000b) fault zones were sampled in a clear structural context (Figs. 2e,h; 3c,d) for subsequent single zircon U–Pb and/or single white mica Rb-Sr microsampling dating.

U–Pb analyses of three single zircons from dyke PEI69 crosscutting the Peio mylonites (Figs. 2e, 3d)

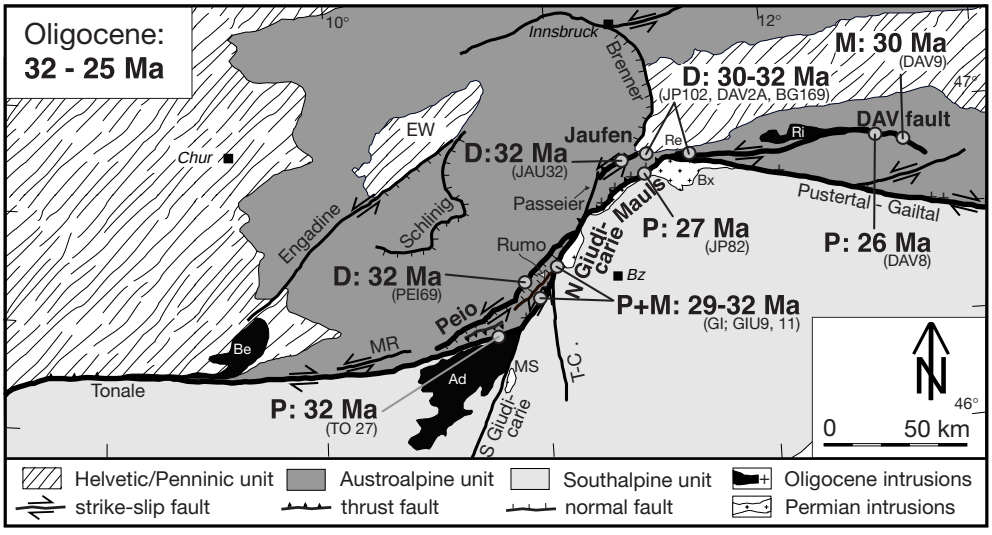

Fig. 10 Simplified tectonic sketch map of the central sector of the PAF. Locations and ages of Oligocene fault rocks and dykes within the fault zones are indicated. *D* dyke single-zircon U–Pb intrusion age. See Figs. 1 and 4 for abbreviations

are concordant with individual ^{238}U-^{206}Pb ages ranging between 32.1 and 31.7 Ma, which almost overlap within respective error limits (Fig. 11a). These ^{238}U–^{206}Pb ages neither correlate with corresponding U concentrations nor with crystal morphology (Table 5). Differing Th/U ratios among the zircons point to variable Th/U in the source, with the observed range of ^{238}U–^{206}Pb ages possibly reflecting small, but real, time differences in crystallization ages rather than cryptic inherited components. Tubular inclusions parallel to the c-axis within zircon Z4 are interpreted as melt inclusions, which argues for Zr supersaturation in the melt, auto-nucleation and therefore inheritance-free zircons (Bossart et al. 1986). A mean age of ~31.9 Ma is inferred for the intrusion of dyke PEI69, which agrees well with other ages of Periadriatic plutons (e.g. Barth et al. 1989; von Blanckenburg et al. 1998). The Peio fault therefore must be older than ~32 Ma, which is in line with ages of mylonites and pseudotachylytes of ~70 Ma (Fig. 4; see above).

A strongly mylonitized dyke was collected within the Jaufen mylonites (JAU32; Figs. 2h, 3c) and its intrusion age places an upper limit on the age of ductile deformation along the Jaufen fault. Five single zircons were analysed by U–Pb (Fig. 11b). Zircons Z3, Z4 and Z6 are discordant and contrast with two concordant zircons Z1 and Z5. This difference is mirrored by low U concentrations and elevated Th/U ratios of Z4 and Z6 (< 470 ppm and > 0.37, respectively), whereas concordant zircons Z1 and Z5 record high U concentrations and low Th/U ratios (>1522 ppm and ~0.036, respectively). A discordia line connecting all five zircons has a lower intercept of 31.7±3.4 Ma and an upper intercept of 527±88 Ma (MSWD=3.1). The lower intercept agrees well with ^{238}U–^{206}Pb ages of both Z1 and Z5 (31.7 and 31.8 Ma) and is therefore interpreted as the intrusion age of JAU32. This age agrees well with the timing of Periadriatic magmatism (von Blanckenburg et al. 1998). Consequently, both sinistral and dextral deformation along the Jaufen fault postdate ~32 Ma. The MSWD of 3.1 for the discordia line indicates scatter outside analytical error, which suggests inhomogeneity among the inherited components.

Dykes BG169, DAV2A and JP102 record strong sinistral solid-state ductile deformation related to the DAV fault (Fig. 10). Two single, large magmatic white

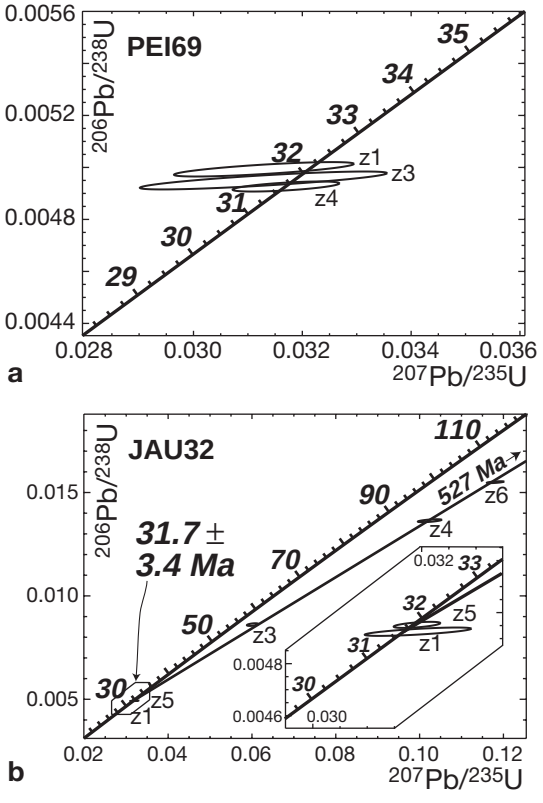

Fig. 11 U–Pb concordia diagrams for dykes **a** PEI69 and **b** JAU32

micas together with adjacent plagioclase from BG169 yielded a Rb–Sr microsampling age of 30.9±0.2 Ma (Müller et al. 2000b). Six single zircons from neighbouring dyke DAV2A were analysed by U–Pb techniques and the corresponding results show scatter in conventional Concordia representation. Because of the combined complexities arising from both inheritance and (deformationally induced) partial resetting of U–Pb systems, no precise emplacement age for the dyke is obtained, but an age of 31–32.5 Ma is most likely (Müller 1998). Two large magmatic white micas and adjacent K-feldspar from the sinistrally deformed dyke JP102 yielded a Rb–Sr microsampling age of 29.9±0.3 Ma (Müller et al. 2000b). Similar to BG169, the age of 29.9 Ma very closely approximates the age of intrusion of this thin dyke (~0.5 m) into relatively shallow crustal levels. Taken together, the ages of these three magmatic dykes suggest that sinistral DAV-related deformation continued until ~30 Ma (see Müller et al. 2000b; Mancktelow et al., this volume). This is in line with a Rb–Sr microsampling age of mylonite DAV9, collected from the southern contact aureole of the Oligocene Rieserferner intrusion. Due to sinistral shearing, contact-related andalusite porphyroblasts are transformed into σ-clasts, where syndeformational growth of white mica occurs. White mica–andalusite pairs yielded a Rb–Sr microsampling age of 30.1±4.6 Ma (Müller et al. 2000b), which is similar to the age of intrusion of the Rieserferner pluton (31±3 Ma; Borsi et al. 1978b).

Ages of fault rocks collected along various PAF-related faults (North Giudicarie, Tonale, Mauls, DAV) provide direct evidence for Oligocene deformation. Significant temporal constraints were obtained from two mylonites (GIU9, GIU11) and one pseudotachylyte (GI) collected along the North Giudicarie fault (Fig. 10). From low-grade basement mylonite GIU9, µg-sized synkinematic chlorite (>100 µm) grown between stretched albite together with newly and/or fully recrystallized white mica (10–20 µm) formed as breakdown product of feldspar were used for Rb–Sr microsampling dating (Figs. 2a, 12a). Due to fairly enriched white mica ($^{87}Rb/^{86}Sr$=23.6), a precise age of 31.6±1.0 Ma was obtained for the chlorite–white mica pair (Fig. 12b), despite the small amounts of Sr analysed (100 and 650 pg, respectively). Fine-grained chlorite and white mica are in full textural equilibrium and thus likely to be isotopically equilibrated, for which the age of 32 Ma is interpreted to reliably date the time of mylonitization. This age is regarded as a formation age because syndeformational temperatures from quartz microstructures are in the range of 250–300 °C, which is below the temperature required for diffusional loss of Sr in both chlorite and white mica (Cliff 1993; Müller et al. 1999). Calcareous mylonite GIU11 was collected ~4 m below GIU9. Rb–Sr analyses of three mineral size fractions (4–6, 2–4, <2 µm) were corrected for their initial $^{87}Sr/^{86}Sr$ ratio using the leachate of the host carbonate. Ages of the three fairly radiogenic size fractions were 29.8±0.2 Ma (4–6 µm), 27.5±0.2 Ma (2–4 µm) and 22.9±0.1 Ma (<2 µm; Fig. 12c). Ages decrease with grain size and are therefore regarded as minimum ages for low-temperature ductile deformation along the North Giudicarie fault. Petrographically, GIU11 is a pure calcareous mylonite and significant detrital/inherited components (e.g. feldspar) can be excluded, as is also

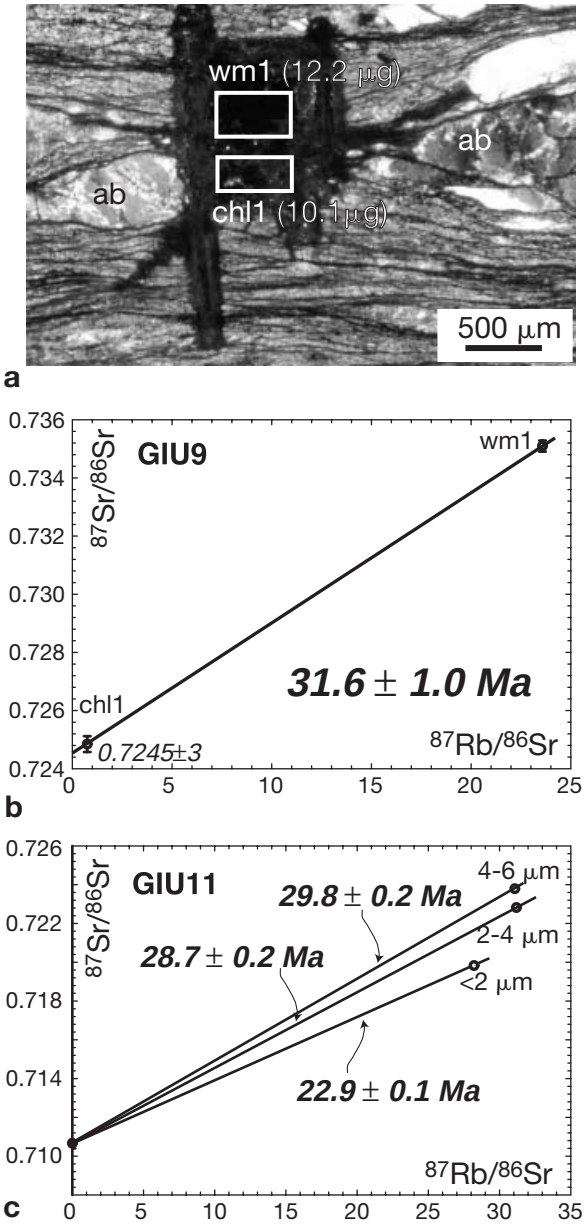

Fig. 12 **a** Thick section of thrust-related, basement-derived, low-grade mylonite GIU9 from the N Giudicarie fault (crossed polarizers; see Figs. 2a, 3a). *White rectangles* indicate size of chlorite and white mica samples after microdrilling and extraction; microdrilling cuts surrounding the *extracted rectangles* are in *black*. **b, c** Rb–Sr microsampling isochron diagrams for mylonites GIU9 and GIU11

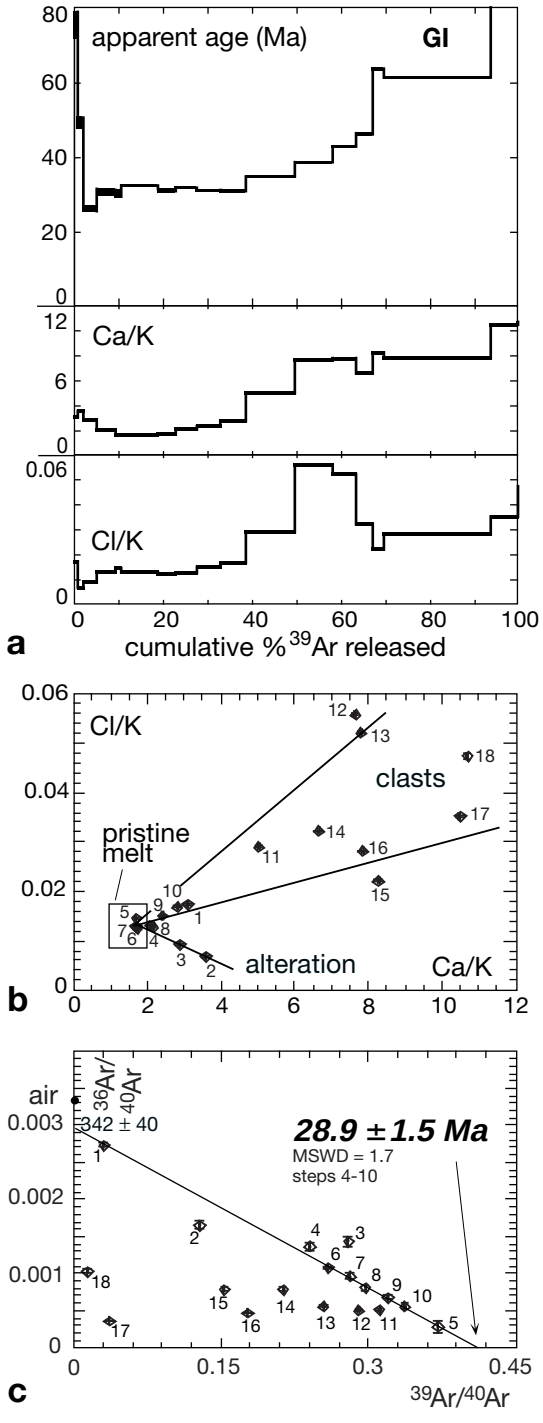

Fig. 13 **a** $^{40}Ar/^{39}Ar$ stepwise-heating spectra, **b** corresponding mineral chemical discrimination diagram based on Ar isotopes, and **c** isochron plot for pseudotachylyte GI from the N Giudicarie fault

indicated by the low Sr concentrations of the mineral size fractions (25–28 ppm). Similarly, the K concentration of 6.1% calculated from $^{40}Ar/^{39}Ar$ analyses of both coarser-grained size fractions argues for fairly pure white mica with some admixture of chlorite and/or quartz. Significant diffusional Sr loss after mineral growth is considered to be unlikely given the low temperatures (<300 °C) of deformation estimated from cogenetic basement mylonites (cf. GIU9). Hence, the most likely explanation is protracted deformation (e.g. Müller et al. 2000a) along the North Giudicarie fault, which has led to later mineral growth and/or alteration within the calcareous mylonites. Such effects would be best seen in the smallest mineral size fraction (<2 μm), which in fact records the youngest age (Fig. 12c).

Pseudotachylyte GI was dated by stepwise-heating $^{40}Ar/^{39}Ar$ and yielded a discordant apparent age spectrum. Steps 1 and 2 show ages >50 Ma, followed by a flat portion with ages around 31 Ma (35% of released ^{39}Ar) and a final increase to ages >100 Ma (60% ^{39}Ar; Fig. 13a). Apart from steps 1 and 2, which are most likely related to later alteration associated with excess argon, two distinct chemical reservoirs are distinguished on the basis of Ar isotope-based chemistry. Low Ca/K and Cl/K ratios characterize the lower-temperature steps, whereas high Cl/K and Ca/K ratios are recorded at higher temperatures. When plotted on a Cl/K–Ca/K diagram, two main mixing trends are evident (Fig. 13b). One trend points towards alteration-related high Ca/K and low Cl/K phases (steps 2–4), the other indicates high Ca/K and high Cl/K phases, i.e. inheritance (clasts). Steps 5–7 lie near the intersection between these mixing trends and are therefore regarded as the best approximation of the pristine pseudotachylyte matrix (melt). They yield an apparent age of 31.2±2.4 Ma, which remains similar, if all "flat" steps (4–10) are considered (31.1±0.6 Ma; 35% ^{39}Ar released). Regressing matrix/melt-related steps 5–7 in an isochron diagram yields an age of 28.6±2.7 Ma ($2\sigma_{ext.}$) with a $^{40}Ar/^{36}Ar$ intercept of 351± 61 (MSWD=1.5), basically overlapping in error with air (Fig. 13c). The result remains identical if extended to steps 4–10 (28.9±1.5 Ma, $^{40}Ar/^{36}Ar$=341±41, MSWD=1.7). The 28.9±1.5-Ma pseudotachylyte age is therefore considered to be reliable and agrees well with ages for North Giudicarie fault mylonites discussed above.

Pseudotachylyte TO27 was collected along an antithetic Riedel fault immediately north of and cogenetic with the eastern Tonale fault (Figs. 3b, 10). It yielded a laser-ablation $^{40}Ar/^{39}Ar$ age of 32.1±3.5 Ma (W. Müller et al., submitted). This age provides direct and independent control for Oligocene dextral deformation along the Tonale fault, which is consistent with submagmatic to high-temperature solid-state deformation within the various Oligocene Periadriatic plutons along the PAF *s. str.* (e.g. Martin et al. 1993; Berger et al. 1996; Sprenger 1996; Nemes 1997). Similarly, the northern contact aureole of the Adamello-Presanella pluton (Fig. 1) records ductile dextral strike-slip deformation related to the northerly adjacent Tonale fault (Werling 1992).

Two pseudotachylytes sampled along the Mauls and DAV faults (JP82 and DAV8, respectively) were analysed by stepwise-heating $^{40}Ar/^{39}Ar$. Host rock of

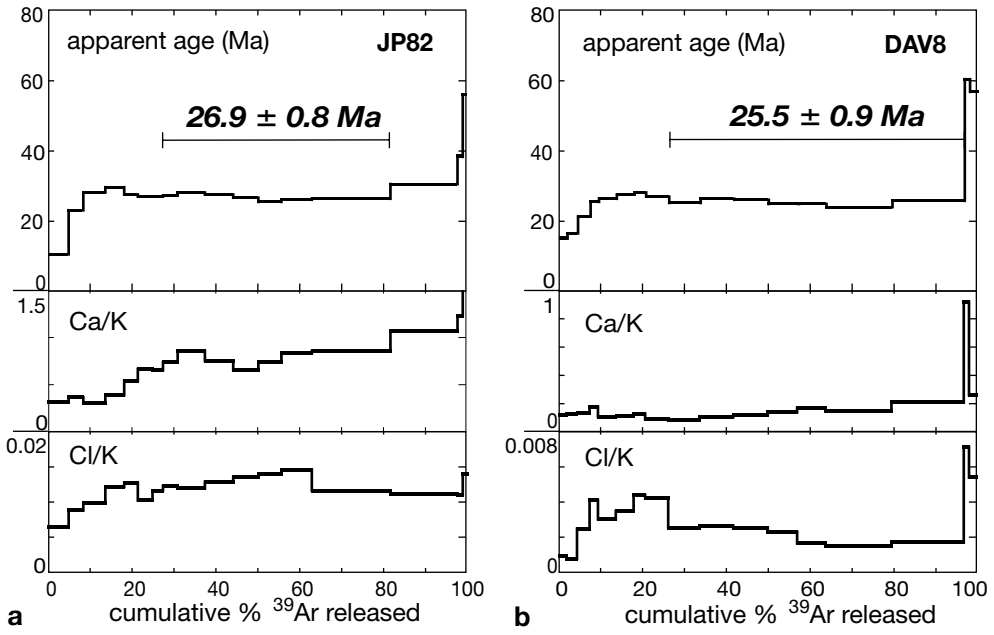

Fig. 14 $^{40}Ar/^{39}Ar$ stepwise-heating spectra for pseudotachylytes **a** JP82 and **b** DAV8

well-preserved pseudotachylyte JP82 (Fig. 2f) is the Oligocene Mauls tonalite (~29–31 Ma; Stöckli 1995; Elias 1998) which provides a maximum age for the pseudotachylyte formation. The age spectrum of JP82 records apparent ages between 10 and 55 Ma. Ages vary between 25 and 30 Ma over ~75% ^{39}Ar released (Fig. 14a). Low Cl/K and Ca/K ratios of low-temperature steps indicate later alteration. The highest Cl/K ratio recorded during step 13 may correlate with the breakdown of matrix biotite (Fig. 2f). The remaining Ar is most likely released from matrix feldspar (step 14; Fig. 2f) and inherited clasts (steps 15–17). The fairly homogeneous composition of steps 8–14 allows the calculation of an age of 26.9±0.8 Ma (~55% ^{39}Ar released). The limited spread in $^{39}Ar/^{40}Ar$ ratio among the steps and residual scatter precludes an age calculation using an isochron. Apparent ages of steps 16 and 17 exceed the Oligocene age of the hosting tonalite. If recoil loss of ^{39}Ar caused the elevated ages, then corresponding Ca/K ratios would decrease concomitantly since ^{37}Ar shows a more than twice as large recoil distance compared with ^{39}Ar (Onstott et al. 1995). Since increasing Ca/K ratios are recorded at highest temperatures, excess ^{40}Ar associated with plagioclase clasts is considered as the source for the old ages (Villa 1983).

Pseudotachylyte DAV8 was collected from the same outcrop as DAV881b (~60 Ma; Fig. 6) S of DAV fault (Fig. 10). The age spectrum of DAV8 records ages between 15 and 60 Ma, with a flat middle portion ranging between 24 and 28 Ma (~90% ^{39}Ar released; Fig. 14b). Cl/K ratios are slightly positively correlated with apparent age, with the highest Cl/K ratios and concomitantly oldest ages released during steps 7 and 8 (breakdown of biotite?). Apart from old ages due to inherited clasts at highest temperatures, the remaining ~70% ^{39}Ar are characterized by fairly similar ages, from which an age of 25.5±0.9 Ma can be calculated.

Early to Middle Miocene (22–15 Ma)

Only pseudotachylytes record the more brittle movements along the PAF during the Miocene (Fig. 15). Results of stepwise-heating $^{40}Ar/^{39}Ar$ analyses of pseudotachylytes from the Tonale (INS4, TO26; Fig. 16) and Passeier faults (JAU13; Fig. 17) are discussed together with ages of pseudotachylytes from the Jaufen (JAU10, JAU34) and Pustertal faults (PAL35B) presented by W. Müller et al. (submitted).

Pseudotachylyte INS4 from the westernmost Tonale fault records a relatively flat stepwise-heating $^{40}Ar/^{39}Ar$ age spectrum over ~85% released ^{39}Ar (except steps 1, 2, 9 and 10; Fig. 16a). On the basis of uniform Ca/K and Cl/K ratios, a weighted mean age of 16.4± 0.8 Ma can be calculated. Old ages and high Ca/K ratios at the highest temperatures are attributed to older clasts, whereas the first two steps are explained by alteration along cracks, since chlorite fillings are visible in thin section (high Cl/K ratio during step 1). Pseudotachylyte TO26 yielded a complex staircase age spectrum with apparent ages increasing from 17 to $\geq$80 Ma (Fig. 16b). Limited variation in Cl/K is in contrast to pronounced differences in Ca/K ratios, in particular for high- and low-temperature increments. Steps 5–10 are characterized by uniform compositions (Fig. 16c). The positive correlation of most steps in a $^{36}Ar/^{39}Ar$–Ca/K plot indicates increasing amounts of trapped (inherited) Ar derived from high-Ca/K

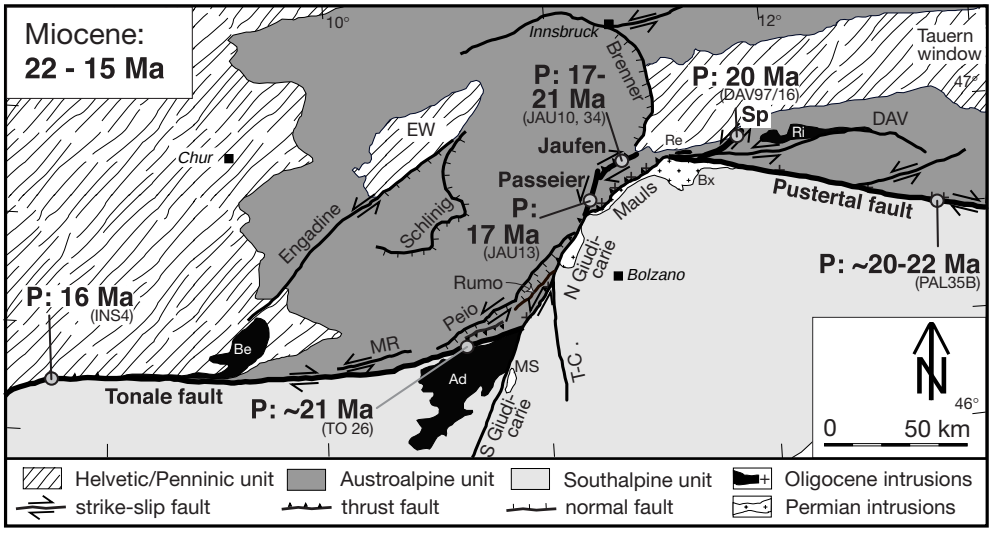

Fig. 15 Simplified tectonic sketch map of the central sector of the PAF. Locations and ages of Miocene pseudotachylytes are indicated. See Figs. 1 and 4 for abbreviations. *Sp* Speikboden fault

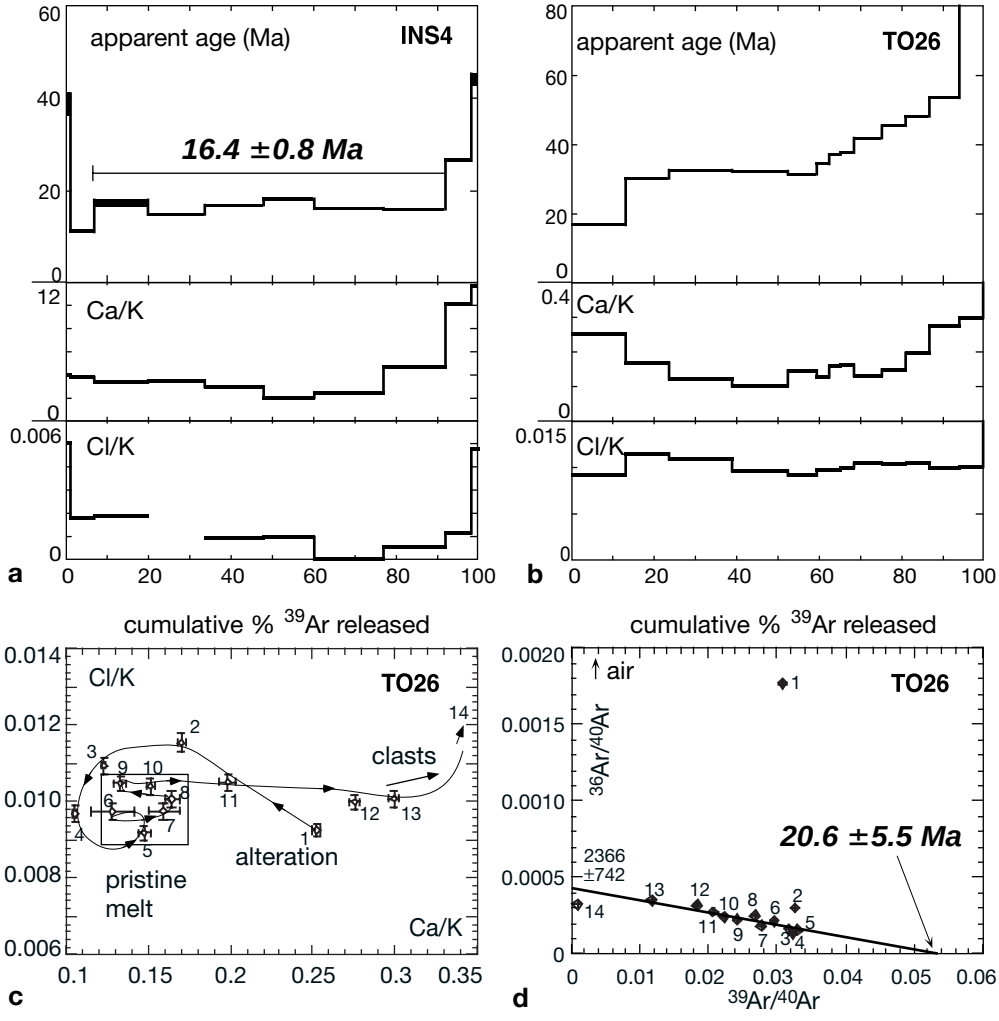

Fig. 16 $^{40}Ar/^{39}Ar$ stepwise-heating spectra for pseudotachylytes **a** INS4 and **b** TO26, **c** corresponding mineral chemical discrimination diagrams based on Ar isotopes and **d** isochron plot for pseudotachylyte TO26

phases, most likely plagioclase (clasts). Incompletely degassed clasts and/or significant incorporation of inherited ^{40}Ar into the melt therefore mask the age information of TO26. Plotted on an isochron diagram, chemically fairly homogeneous steps 5–10 yield an imprecise age of 20.6±5.5 Ma and a $^{40}Ar/^{36}Ar$ ratio of 2366±742 (MSWD=8.4; Fig. 16d). When steps 3 and 4 are also included, the age becomes 22.5±3.4 Ma ($^{40}Ar/$

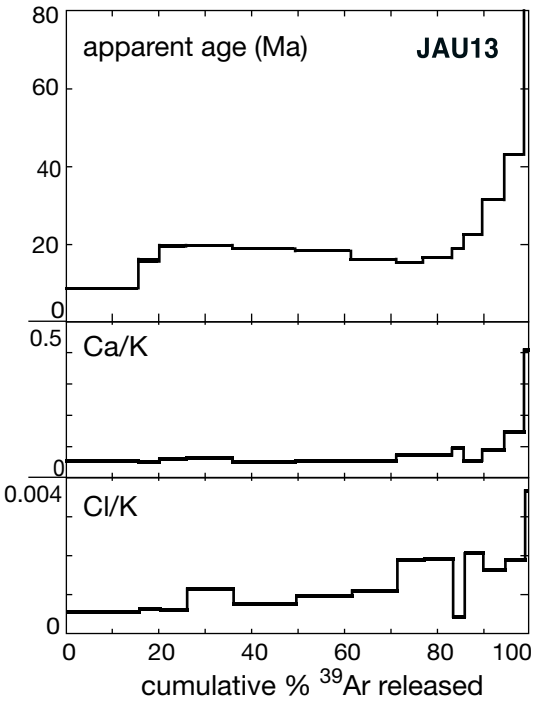

Fig. 17 $^{40}Ar/^{39}Ar$ stepwise-heating spectra for pseudotachylyte JAU13

^{36}Ar ratio=2191±250, MSWD=14.9). Stepwise-heating and laser-ablation analyses were performed from both fault and injection vein of pseudotachylyte PAL35B. Despite complex internal systematics, an age of ~20–22 Ma is inferred (Müller 1998). A pseudotachylyte from the Speikboden mylonite zone, which is interpreted as an antithetic Riedel structure to the coeval Pustertal fault, yielded a stepwise-heating ^{40}Ar–^{39}Ar age of 20.4±1.1 Ma (Mancktelow et al., this volume).

Pseudotachylyte JAU13 was collected along the Passeier fault, which transfers the sinistral strike-slip displacement of the North Giudicarie fault to the north (Fig. 15; Viola 2000). The apparent age spectrum of pseudotachylyte JAU13 records ages between 9 and 510 Ma and a relatively flat middle portion with ages between 15 and 20 Ma (~70% ^{39}Ar released; Fig. 17). The chemical discrimination plots clearly indicate the presence of inherited clasts in steps 11–15 associated with high Ca/K, high Cl/K ratios and old ages. Step 1, and possibly step 2, reveals the effects of later alteration. For the remaining ~70% Ar, a slightly negative correlation between Cl/K ratios and ages and no trend between Ca/K ratios and ages is observed. The former correlation may indicate incipient signs of alteration. From steps 3–10, an age of 17.3±1.1 Ma can be calculated. The Jaufen fault shares a common late brittle dextral kinematic history with the adjacent Mauls faults to the south (Glutz 1997; Meier 1997; Parolini 1997). Two pseudotachylytes from the Jaufen fault (JAU10 and JAU34; Fig. 17) yielded stepwise-heating and laser-ablation $^{40}Ar/^{39}Ar$ ages between 17 and 21 Ma (W. Müller et al., submitted).

Discussion and interpretation

The new geochronological data on fault rocks, available for the first time for the broadly defined Periadriatic fault system, establish a long history of fault activity, lasting from (at least) the Late Cretaceous to the Middle Miocene (Figs. 4, 8, 10, 15, 18). These fault ages allow for a better understanding of the central sector of the PAF.

Oligocene ages (29–32 Ma) of mylonites and pseudotachylytes demonstrate that top-to-(E)SE thrusting along the North Giudicarie fault occurred contemporaneously with dextral strike-slip movements along the Tonale and Pustertal-Gailtal faults (Fig. 1). The observed thrust geometry with a down-dip lineation along the southern part of the North Giudicarie fault (Figs. 3a, 10, 12) cannot be produced by later rotation of an existing dextral strike-slip fault and, in contrast, there is no indication for a significant thrust component along the eastern Tonale fault (e.g. Werling 1992). Consequently, the combination of established kinematics and direct age control presented here indicates that at least part of the sinistral stepover represented by the North Giudicarie fault formed a cogenetic restraining bend in the dextral PAF (Fig. 1). It could be proposed that the Periadriatic fault was offset in a two-stage process, first by broad bending and then by discrete sinistral strike-slip; however, this does not explain the observed difference in kinematics (coeval dextral strike-slip and (E)SE-directed thrusting) discussed previously. The new ages of fault rocks are consistent with Oligocene biotite Rb–Sr ages of thin tonalite "lamellae" along the North Giudicarie fault, which record magmatic flow and solid-state deformation processes (Martin et al. 1993). Based on different Mesozoic sedimentary facies on either side of the Giudicarie fault, Castellarin and Vai (1981), Picotti et al. (1995) and Prosser (1998) argued that the Giudicarie fault represents an inherited structure formed by inversion of an old, Mesozoic synsedimentary normal fault. Reconstructions of the southern European plate margin by, for example, Weissert and Bernoulli (1985) also suggest the presence of Mesozoic sinistral stepovers. After restoration of ~30-km sinistral strike-slip deduced from the amount of shortening in the kinematically linked Val Trompia thrust belt (e.g. Prosser 1998) and the distribution of the tonalite "lamaelle" along the Giudicarie fault (for discussion see Viola 2000), the transpressive sinistral stepover represented by the North Giudicarie fault still remains as a dominant structural feature of the pre-Miocene PAF.

The primary, i.e. Oligocene or even older (e.g. Picotti et al. 1995), sinistral stepover represented by the North Giudicarie fault places restrictions on the amount of dextral strike-slip accumulated along the

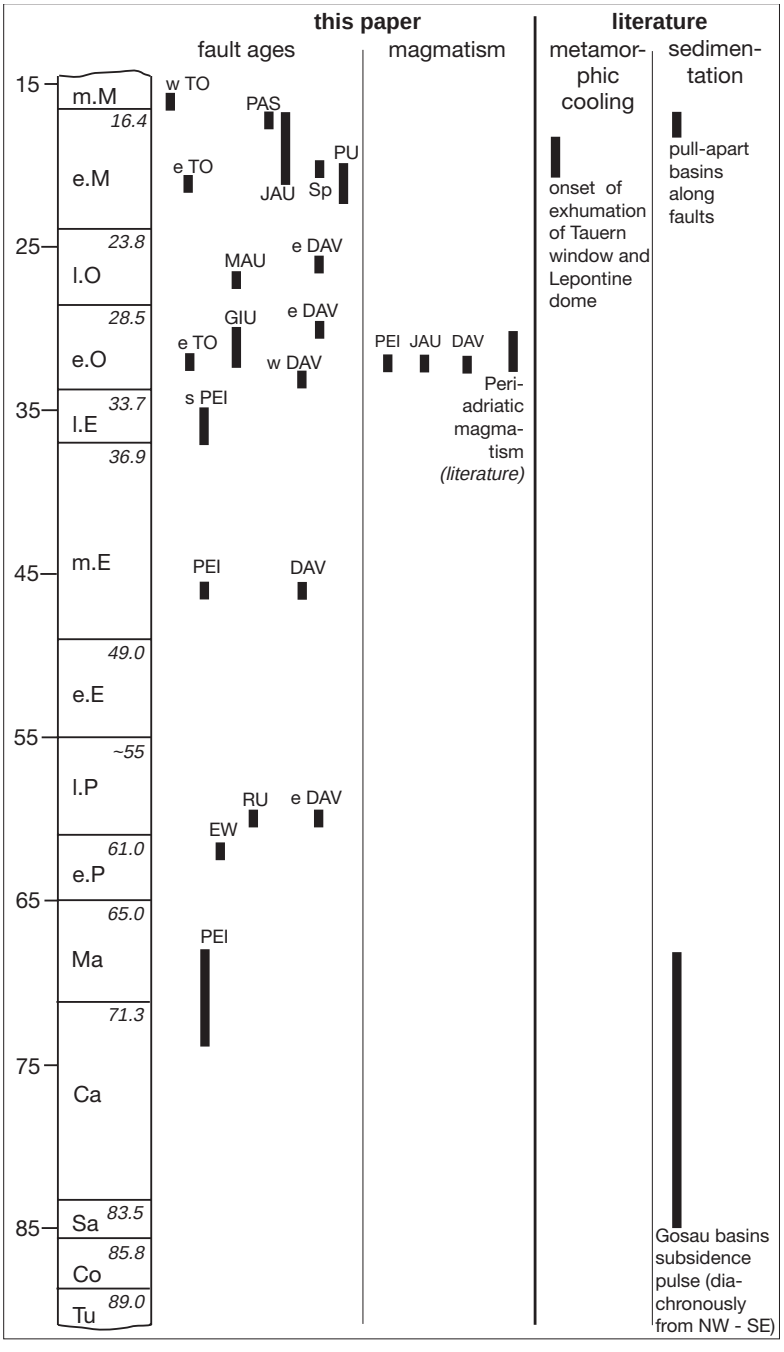

Fig. 18 Schematic sequence of faulting events plotted into the chronostratigraphic time table. Related magmatic, metamorphic and sedimentary events are shown for comparison. See text for details and references. *l* late; *m* middle; *e* early; *M* Miocene; *O* Oligocene; *E* Eocene; *P* Paleocene; *Ma* Maastrichtian; *Ca* Campanian; *Sa* Santonian; *Co* Coniacian; *Tu* Turonian. *JAU* Jaufen; *TO* Tonale; *PAS* Passeier; *PU* Pustertal; *GIU* N Giudicarie; *MAU* Mauls; *DAV* Defereggen-Antholz-Vals; *PEI* Peio; *RU* Rumo; *Sp* Speikboden; *EW* Engadine window; *w* western; *s* southern; *e* eastern

Tonale and (less dramatically) along the Pustertal-Gailtal faults. Previously, the Oligocene Tonale-Pustertal fault was often considered as a straight dextral strike-slip fault with up to 300 km dextral movement that was offset sinistrally during the Middle to Late Miocene (e.g. Laubscher 1988; Ratschbacher et al. 1991; Werling 1992; Frisch et al. 1998). Detailed structural analysis of the North Giudicarie fault by Prosser (1998, 2000), however, established the presence of ductile mylonites with thrust geometry of inferred Late Oligocene to Early Miocene age, which have been dated here at 29–32 Ma (Fig. 12). Syndeformational temperatures of $\leq 300\,^{\circ}C$ within both basement-derived and calcareous mylonites in the hangingwall and ~160–170 °C within the underlying Cretaceous Insubric flysch (Hennig 1991; Martin et al. 1993; Prosser 1998) indicate a jump of ~100–150 °C in metamorphic conditions across the North Giudicarie fault. If converted to depth using an average geothermal gradient of 30 °C/km, the footwall would have been buried under an ~4- to 6-km-thick hangingwall slab composed of Austroalpine unit rocks. Using an

average dip of the North Giudicarie mylonites of ~30° towards NW (315°) as recorded in the sampled section, the 6-km vertical component of displacement can be converted to ~11-km horizontal component during thrusting. Even if the mylonites had shallower dip angles of, for example, ~10°, the horizontal component would still be only ~35 km. All these estimates are affected by various, not readily assessable sources of error, which include the uncertainty of metamorphic temperatures, the original dip angle of the North Giudicarie fault, and the amount of shortening within both footwall and hangingwall, among others. However, the moderate jump in metamorphic grade across the North Giudicarie thrust is well established and does not allow for more than ~30-km horizontal displacement. This also limits the horizontal displacement along the kinematically linked Tonale fault to less than ~30–40 km, which is significantly less than the values commonly assumed (e.g. 100 km; Schmid and Kissling 2000). This result bears comparison with, for example, Ahrendt (1980), who deduced approximately 20- to 40-km dextral displacement from the position of the Bergell pluton and related boulders in molasse deposits to the S (Fig. 1, "Be" and "M").

The Peio fault located N(W) of the Tonale and North Giudicarie faults has been suggested as another possible fault system responsible for transferring dextral movements between the Tonale and the Pustertal faults (e.g. Laubscher 1970; Schmid et al. 1989). Both sinistral fault transtensive kinematics (e.g. Martin et al. 1991; Werling 1992) and the now established Late Cretaceous age of mylonites and pseudotachylytes along the Peio fault (74–67 Ma; Fig. 4) are incompatible with this transfer model. These Late Cretaceous fault ages are in line with K/Ar ages of mineral size fractions (<2 and <6.3 μm) from Peio fault mylonites ranging between 70 and 55 Ma (Schäfer 1989; Zarske 1989). A dyke crosscutting the Peio mylonites (Berger 1989; Werling 1992) yielded an age of 32 Ma (Fig. 11a) and provides independent evidence for pre-Oligocene activity along the Peio fault. A Middle Eocene pseudotachylyte (46 Ma; Fig. 9) and two K/Ar ages of mineral size fractions (41+33 Ma; Schäfer 1989; Zarske 1989) indicate some later reactivation of the main mylonite zone of the Peio fault. Shear zones S of the Peio fault characterized by opposite top-to-(W)NW thrusting have overlapping mylonite and pseudotachylyte ages in the range 37 to 35 Ma (Fig. 8; W. Müller et al., submitted).

In addition to Late Cretaceous sinistral transtensive movements along the Peio fault, a few Paleocene pseudotachylyte ages (~60 Ma) have also been found for other faults characterized by extensional movements (Fig. 4; Rumo fault, S of DAV fault, basal Silvretta nappe). These data suggest pronounced latest Cretaceous–Paleocene extension within the Austroalpine unit following Eoalpine (i.e. mid-Cretaceous, 90–85 Ma; Frank et al. 1987; Thöni 1999) metamorphism and thrusting (e.g. Fügenschuh 1995; Neubauer et al. 1995). Froitzheim et al. (1997) suggest that Late Cretaceous extension is related to westward rollback of the subduction boundary, leading to ESE-dipping normal faults in the Austroalpine nappes, and sinistral shearing along forerunners of the Tertiary PAF.

The Jaufen fault has had a complex history of multiple reactivation (Fig. 15). Late Cretaceous amphibolite facies metamorphism to the N is juxtaposed against Alpine weakly metamorphic units to the S suggesting significant post-late Cretaceous north-side-up displacement (e.g. Spiess 1995). However, the displacement kinematics determined from the ~200-m-thick mylonitic belt show first a sinistral, south-side-up deformational event followed by dextral low-grade mylonites and cataclasites (Glutz 1997; Parolini 1997). The Oligocene age (32 Ma) of the mylonitized dyke within the Jaufen mylonites (Fig. 11b) demonstrates that both sinistral and dextral deformation are younger than 32 Ma. No evidence for earlier deformation responsible for the observed jump in ages is seen along the present Jaufen fault, possibly because of strong overprint during post-32 Ma deformation. The youngest, brittle, dextral deformation is kinematically linked to the PAF *s. str.* as deduced from both similar kinematics and pseudotachylyte ages between 17 and 21 Ma (Figs. 15, 17).

Comparison with the sedimentary record

Late Cretaceous sedimentary basins (Gosau Group) occur within the Upper Austroalpine Northern Calcareous Alps and as isolated occurrences on the metamorphosed Austroalpine basement E of the Tauern window (Fig. 1, "Go"; Wagreich and Faupl 1994; Neubauer et al. 1995). Late Turonian to Early Campanian fluviatile to shallow marine deposits (~90–82 Ma) unconformably seal older thrust-related structures, which are in turn overlain by deep-water facies, turbiditic sediments of Late Campanian to Paleocene age (~75–60 Ma). The deep-water facies is initiated by a pronounced subsidence pulse occurring diachronously from NW to SE between the Turonian/Coniacian to the Maastrichtian (~89 to ~68 Ma; Wagreich and Faupl 1994). Gosau basins located upon the Austroalpine basement ("Centralalpine" Gosau) show a slightly different evolution starting with a Santonian/Campanian transgression followed by Maastrichtian deep-water sediments (Neubauer et al. 1995). The second, major subsidence of the Gosau Group to deep-water facies may be correlated with Late Cretaceous extensional faults, as suggested by Neubauer et al. (1995) for the eastern Centralalpine Gosau. The timing for such normal faults established during this study (74–67 Ma for the Peio fault and Paleocene activity elsewhere; Fig. 4) fits well with this tectonic scenario (see also Froitzheim et al. 1997).

Early to Middle Miocene pseudotachylyte formation along the PAF can be correlated with contem-

poraneous sedimentation at fault-bound basins. During the Early to Middle Miocene, orogen-parallel extension is known from both the Central and Eastern Alps (e.g. Mancktelow 1992; Behrmann 1988; Selverstone 1988; Neubauer and Genser 1990), for the latter by a process of "lateral extrusion" (Ratschbacher et al. 1991). The laterally extruding wedge of the Eastern Alps is bounded by a northern sinistral fault system comprising the Salzachtal-Ennstal fault and the Mur-Mürz fault, with pull-apart basins frequently occurring along releasing stepovers (Fig. 1). The dextral PAF *s. str.* and related faults, such as the Lavanttal fault, represent the southern border of the extruding wedge. Two independent observations provide constraints on the timing of this orogen-parallel extension (Ratschbacher et al. 1991; Decker and Peresson 1996; Frisch et al. 1998). Firstly, syndeformational basins along the faults related to this system initiated during the Early–Middle Miocene (Karpatian; ~17 Ma). Secondly, extension-driven exhumation of metamorphic domes, such as the Lepontine dome and the Tauern window, started ~20–18 Ma ago, as modelled from mineral cooling ages (von Blanckenburg et al. 1989; Mancktelow 1992; Grasemann and Mancktelow 1993; Fügenschuh et al. 1997). The $^{40}Ar/^{39}Ar$ ages of pseudotachylytes in the range of 22–16 Ma (Fig. 17) along the Tonale, Pustertal and the kinematically linked Jaufen and Passeier faults provide the first direct evidence from fault rocks for widespread Early Miocene faulting consistent with the model for lateral extrusion.

Conclusion

The application of microsampling techniques (Rb–Sr and $^{40}Ar/^{39}Ar$) for the dating of mylonites and pseudotachylytes is capable of reliably constraining the age of faulting. For the different faults that comprise the Periadriatic fault system, a long-lasting history from Late Cretaceous to Middle Miocene was established using these methods.

For the central sector of the PAF, Oligocene thrust-related mylonites and pseudotachylytes along the North Giudicarie fault (29–32 Ma) place a limit on the extent of dextral strike-slip along the kinematically linked Tonale fault. Contrary to previous estimates, a maximum of ~ 30 km of dextral displacement follows from this interpretation. The Tonale and Pustertal faults did not originally form a straight dextral fault zone, but were connected via a dextrally transpressive restraining bend, represented by the North Giudicarie fault. The Peio fault is not part of a dextral transfer system between the Tonale and Pustertal faults because of its Late Cretaceous age of faulting and sinistral sense of shear. Together with Paleocene pseudotachylytes along other PAF-related faults, a major extensional phase is directly dated to be Late Cretaceous–Paleocene in age. The sedimentary record of contemporaneous Gosau Group sediments suggests a genetic link between sedimentation and normal faulting. Miocene pseudotachylytes along the PAF coincide with the timing for lateral extension (extrusion) of the Central and Eastern Alps as deduced from syndeformational sedimentary deposits.

Appendix A: Sample description

Detailed locations of the samples presented are listed in Table 1. Locations of other samples discussed herein are in Müller et al. (2000b), Müller (1998) and in a forthcoming article by W. Müller et al.

Tonale-Pustertal fault

Four pseudotachylytes were collected from different locations along the Tonale and Pustertal faults (Figs. 1, 15). Pseudotachylyte INS4 was collected from an impressive outcrop along the westernmost Tonale fault, where many thick (up to 10 cm) pseudotachylytes intrude a high-grade paragneiss of the Ivrea zone. It is a dark-grey, ~10 cm-thick fault vein, which also intrudes the host rock along thin injection veins (0.5–1 cm wide). Numerous rounded clasts composed of quartz and lithic fragments show different degrees of resorption by the melt and are embedded in a fine-grained matrix. The matrix is too fine grained to be optically resolved, but ~10 μm-long laths of ore minerals are identified.

Pseudotachylyte TO26 was sampled from the ~100-m-wide cataclasite zone of the eastern Tonale fault N of the Adamello-Presanella intrusion (Figs. 1, 15). The outcrop is strongly overprinted by brittle faults and joints, which made sample preparation and drilling difficult. TO26 is a ~1 cm-thick fault vein with small injection veins. The brown matrix displays lithological banding parallel to the margins. Melt inflow into the injection veins is locally observed. Variably rounded quartz and a few feldspar clasts (<150 μm) occur. The matrix is too fine grained to be optically examined. Pseudotachylyte TO27 was collected along an antithetic Riedel fault immediately north of and cogenetic with the eastern Tonale fault (Fig. 3b). It is a <4 mm-wide injection vein hosted by a retrogressed paragneiss of the Tonale unit. (Details will appear in a forthcoming article by W. Müller et al.).

Pseudotachylyte PAL35B was collected from a spectacular outcrop of the Pustertal fault, where green volcanics are intercalated with ?Ordovician-Silurian shales (for details see Müller 1998). PAL35B is an ~2- to 3 cm-thick, black fault vein with ~0.5 cm-wide injection veins along en echelon feather cracks (Riedel geometry).

North Giudicarie fault and Mauls fault

Two mylonites were sampled in the Proveis/Proves section of the North Giudicarie fault (Prosser 1998). Due to intense mylonitization with a top-to-(E)SE thrust sense of movement (Fig. 3a), the pre-Alpine high-grade Tonale basement is characterized by a strong low-grade retrogression in a zone ~10–20 m above the Giudicarie fault. The fault itself is marked by carbonate mylonites in the Proveis profile. Mylonite GIU9 was collected from low-grade basement mylonites ~2 m above the contact to the underlying calcareous mylonites (Figs. 1, 10). In response to the mylonitization, new chlorite and quartz fibres grow in between the separated feldspar fragments (Fig. 2a). Such chlorite, together with immediately adjacent, newly formed white mica, was used for dating of mylonitization. Deformation occurred at the lower limit of quartz ductility, as shown by incipient recrystallization via subgrain rotation, for which syndeformational temperatures of 250–300 °C are estimated. A band of 50- to 100 m-thick calcareous mylonites occurs in the immediate footwall of the basement mylonites (Prosser 1998). Calcareous mylonite GIU11 was taken ~2 m below the contact, and has a similar geometry with regard to foliation and lineation as GIU9. Top-to-(S)E sense of shear can be inferred from macroscopic σ-type clasts (Fig. 2b).

A pseudotachylyte, referred to as GI, was collected along the southern part of the North Giudicarie fault (near Castello di Altaguardia). The pseudotachylyte forms both fault and injection veins; the latter (~1 cm wide) were used for stepwise-heating $^{40}Ar/^{39}Ar$ analysis. The pseudotachylyte exhibits a sharp and very fine-grained margin with matrix minerals <10 μm that gradually becomes coarser towards the centre of the vein with randomly oriented, ~30 μm sized minerals. The matrix contains abundant clasts composed of plagioclase, epidote or lithic fragments (~500 μm), which are often partially resorbed. No amphibole clasts occur. Apart from later cracks filled with epidote/clinozoisite, no alteration of the pristine matrix is observed.

Along the Mauls fault, a thin ($\leq$400 m wide) foliated Oligocene tonalite lamella occurs along the northern boundary of the Permian Brixen intrusion (Fig. 1; Stöckli 1995; Meier 1997; Elias 1998). The tonalite is strongly faulted, resulting in both frequent cataclasites and rare pseudotachylytes. Pseudotachylyte JP82 is a black and 2- to 3 cm-thick fault vein, which does not show significant veining into the hosting tonalite. In thin section, a textbook example of pseudotachylyte texture is observed (Fig. 2f). The tonalite is strongly cataclastically deformed along a 2- to 5 mm-wide zone between the pseudotachylyte and the undeformed host rock (grain size >1 mm). This cataclasite contains angular clasts (~100 μm) composed of all tonalite minerals (including biotite and hornblende) that are all embedded in a fine-grained matrix. The margin of the pseudotachylyte (~2 mm) is black, very fine grained (<1 μm) and resembles a chilled margin. Many rounded and partially resorbed clasts with concave grain boundaries indicative for melt contact occur within the pseudotachylyte margin. Cataclasite clasts demonstrate preceding brittle deformation. Towards the interior of the pseudotachylyte vein, fewer clasts occur (mostly quartz and some plagioclase) and the matrix becomes gradually coarser grained. Tiny (<40 μm) biotite needles (microlites) nucleate at clasts, forming radial textures. Rare plagioclase and biotite microlites (grain size <120 μm) grow into lithic clasts and form amygdales (Fig. 2f; Maddock et al. 1987). From the occurrence of plagioclase microlites coexisting with biotite and the overall texture of JP82, it is concluded that the matrix has crystallized from a melt. This microlite domain was used for stepwise-heating $^{40}Ar/^{39}Ar$ analyses. Apart from a few joints no significant alteration is observed.

Rumo fault

Two pseudotachylytes (RU23 and RU24) were collected at one spectacular outcrop of the Rumo fault, which contains several thick pseudotachylyte veins forming an anastomosing pattern of fault and injection veins (Fig. 2g). They are hosted by a strongly retrogressed paragneiss. Macroscopically, flow structures within the ~5 cm thick pseudotachylyte veins are evident. The brownish matrix of both pseudotachylytes is microcrystalline and forms a fine-grained network (<3 μm) of presumably mica and plagioclase in which strongly undulose, resorbed quartz clasts are embedded. Chilled margin-like structures are developed along the wall-rock contacts of thin injection veins.

Peio fault (s.l.)

Two pseudotachylytes (PEI49, PEI52) and one ultramylonite (PEI53) were sampled from a single outcrop within the immediate footwall of the Peio fault (Figs. 1, 4). Because of the methodological implications for dating pseudotachylytes, the results of this peculiar association of fault rocks will be presented elsewhere (W. Müller et al., submitted) and only their regional implications are discussed herein.

Another pseudotachylyte (PEI74) was collected from the "Forcellina di Montozzo" section (Werling 1992) within the immediate footwall of the Peio fault. It is an ~3 cm thick fault vein parallel to the mylonitic foliation, from which several injection veins branch off. They crosscut the mylonitic foliation and do not show any signs of later deformation. Structures indicative of melt inflow into the injection veins are observed macroscopically. The matrix contains relatively few, rounded clasts (quartz and albite;

<100 μm) showing variable degrees of resorption by the melt and a few, millimetre-sized lithic clasts mainly composed of recrystallized quartz. In the centre of the pseudotachylyte vein, a very fine-grained (<3 μm) pristine matrix occurs, which along the contact to the host rock appears to be slightly recrystallized. The thick section for laser-ablation $^{40}Ar/^{39}Ar$ analyses was taken from the interior, pristine part of the pseudotachylyte.

Dyke PEI69 was sampled N of Alplanersee (Figs. 1, 10). It clearly crosscuts the Peio fault related mylonites and thus provides a lower limit for the age of mylonitization (Figs. 2e, 3d; Berger 1989; Werling 1992). Open folding affects both dyke and adjacent mylonites and postdates both intrusion and mylonitization.

Two pseudotachylytes (PEI12, PEI26) and two mylonites (PEI27, PEI33), all showing similar fault geometries, were sampled along slightly more steeply dipping, discrete low-temperature shear zones immediately to the south of the Peio fault. Results and details of these four faults rocks are presented in a forthcoming article by W. Müller et al., and only their regional implications are discussed herein.

Jaufen and Passeier faults

During field work for this study, several magmatic dykes were discovered within the mylonite zone of the Jaufen fault (Fig. 3d). Because of their strong mylonitization (Fig. 2h), their magmatic age provides a maximum age for pervasive, sinistral ductile deformation (i.e. the first observable deformation phase) along the Jaufen fault. Similar dykes within the Jaufen mylonites ~2 km further to the W are strongly mylonitized, with a NW-plunging lineation and moderately N(N)W dipping foliation. Sense of shear is sinistral and S-side-up (Fig. 3c). Although no direct evidence for sinistral deformation was found for the dated dyke JAU32, the similarity in geometry and composition argues that JAU32 was deformed with the same kinematics. Both host rock and dyke JAU32 are strongly overprinted by semiductile to brittle N(NE)-dipping dextral faults.

Two pseudotachylytes, JAU10 and JAU34, were collected from one outcrop along the Jaufen fault, and are closely associated with cataclasites and low-grade mylonites, all showing dextral sense of shear similar to the Mauls fault ~7 km further to the SE (Figs. 1, 15). The pseudotachylytes are both fairly thin (<10 mm) and clast laden and hosted by an orthogneiss. Pristine matrix is found mainly in the centre of the veins, whereas incipient recrystallization takes place along the contacts to the wall rock (Details will appear in a forthcoming article by W. Müller et al.).

Pseudotachylyte JAU13 was collected from an outcrop ~350 m W of the Passeier fault (Figs. 1, 15). JAU13 is a thin injection vein hosted by a coarse-grained paragneiss. The brown matrix contains many rounded clasts composed of quartz and cataclastic lithic clasts, which show different degrees of resorption by the melt. The matrix is fine grained (<5 μm) and appears to be slightly recrystallized along the margins, but flow structures are still recognized. In addition, thin cataclasites occur along the margins of the pseudotachylyte.

DAV fault

Two pseudotachylytes, DAV881b and DAV8, were collected from one large outcrop ~1.5 km S of the DAV fault (Figs. 1, 4, 10). Sample DAV881b was supplied by Schulz (1989) and no information on its orientation is available. DAV881b is a ~5 mm thick, clast-laden fault vein showing small injection veins which intrude the host rock. The second pseudotachylyte DAV8 was generated along moderately S(E)-dipping fault planes parallel to the foliation of the hosting orthogneiss. DAV8 consists of two distinct pseudotachylyte generations. The analysed sample was taken from the second, younger generation (Fig. 2i).

Petrographic details of DAV-related dykes and mylonites (BG169, DAV2A, JP102; BG55, DAV9) discussed herein are given by Müller et al. (2000b).

Appendix B: Methodology

Fault rocks, i.e. mylonites and pseudotachylytes, were dated using microsampling techniques. These include Rb–Sr microsampling dating of synkinematic mica from mylonites and both laser-ablation and stepwise-heating $^{40}Ar/^{39}Ar$ dating of pseudotachylytes; for the latter, ~1 mm drill cores were used. Analytical details of these recently developed/improved techniques are in Müller et al. (2000b), Müller (1998) and in a forthcoming article by W. Müller et al..

Calcareous mylonites from the North Giudicarie fault were reduced to small pieces with a hammer and dissolved in dilute acetic acid (~3 M) for ~2 weeks. Subsequent grain-size separation of the insoluble residue into size fraction of 4–6, 2–4 and <2 μm was performed using standard sedimentation techniques (Atterberg cylinder, centrifuge). Part of the same sample (<300 μm) was ultrasonically dissolved in ~3 M acetic acid (3 h), subsequently centrifuged and used for initial $^{87}Sr/^{86}Sr$-ratio correction of the mineral size fractions.

Both undeformed (PEI69) and mylonitized (JAU32, DAV2A) magmatic dykes within the Peio, Jaufen and DAV fault zones were dated by single-zircon U–Pb techniques. Samples were crushed, sieved and a zircon concentrate was obtained using a Wilfley table, heavy liquids and a FRANTZ magnetic separator. After preselection under the binocular microscope, zircon crystals were examined by transmitted

light microscopy. Whenever possible, euhedral, clear grains devoid of indications for optically visible cores (e.g. three-dimensional arrays of bubbles) or cracks were chosen for analysis. Selected zircons were classified after Pupin (1980), photographed and subjected to stepwise air abrasion. U–Pb chemical and mass spectrometric procedures followed Meier and Oberli in Wiedenbeck et al. (1995). Isotopic analyses of U and Pb were performed with both a Varian MAT Tandem mass-spectrometer using an SEM operated in analogue mode and with a MAT 262 RPQ_{plus} mass spectrometer using a RPQ-SEM operated in ion-counting mode. Pb runs were corrected for mass fractionation using a factor of 0.7±0.4‰, whereas U fractionation was corrected using a double-spike procedure. Pb blanks were 4.3±1.0 pg (n=6, $^{208}Pb/^{206}Pb$=2.063±0.012, $^{207}Pb/^{206}Pb$=0.8475±0.0067, $^{204}Pb/^{206}Pb$=0.05401±0.0009) for JAU32 z1, z3, z4, z5, z6, PEI69 z1, z3 and 1.1±0.2 pg (n=2; $^{208}Pb/^{206}Pb$=2.054±0.012, $^{207}Pb/^{206}Pb$=0.8427±0.0067, $^{204}Pb/^{206}Pb$=0.05378±0.0009) for PEI69 z4 (errors are 1σ). Correction for sample common Pb was based on: $^{208}Pb/^{204}Pb$=38.828, $^{207}Pb/^{204}Pb$=15.668, $^{206}Pb/^{204}Pb$=18.771, T=32 Ma (Cumming and Richards 1975; model III).

Constants used are those from Steiger and Jäger (1977). The time scales used for chronostratigraphic correlations are from Gradstein et al. (1994) for the Mesozoic and Berggren et al. (1995) for the Cenozoic. All quoted errors are 95% $c.l._{ext.}$, except when otherwise stated. Abbreviations of mineral names follow Kretz (1983) with the addition of "wm" to indicate "white mica".

Acknowledgements Financial support from ETH grant 0-20-797-94 is gratefully acknowledged. We thank B. Grollimund, D. Stöckli, B. Schulz, and R. Spiess for discussion and help in the field, M.-T. Bär, H. Derksen and M. Meier for their support with lab work, and E. Schärli and A. Willi for the preparation of thick sections. Thanks to K. Kunze for his help with SEM imaging of pseudotachylytes, and to J.-A. Wartho for her help with laser $^{40}Ar/^{39}Ar$ work. Discussions with R.H. Steiger helped to improve this work. B. Schulz and M. Thöni supplied pseudotachylyte samples, which is gratefully acknowledged. A. Del Moro is thanked for making his unpublished geochronological data available. Careful and thorough reviews by M. Thöni and particularly S. Schmid helped to improve the paper and the style of its presentation and are greatly appreciated.

References

Ahrendt H (1980) Die Bedeutung der Insubrischen Linie für den tektonischen Bau der Alpen. N Jahrb Geol Paläontol Abh 160:336–362

Argand E (1916) Sur l'arc des Alpes Occidentales. Eclog Geol Helv 14:145–191

Barth S, Oberli F, Meier M (1989) U–Th–Pb systematics of morphologically characterized zircon and allanite: a high-resolution isotopic study of the Alpine Rensen pluton (northern Italy). Earth Planet Sci Lett 95:235–254

Bauer F, Schermann O (1984) Das Periadriatische Lineament in den Karawanken. Jahrb Geol Bundesanstalt Wien 127:299–305

Behrmann J (1988) Crustal-scale extension in a convergent orogen: the Sterzing-Steinach mylonite zone in the Eastern Alps. Geodin Acta 2:63–73

Berger A (1989) Petrographische und strukturelle Kartierung im mittleren Kirchbergtal (Südtirol, Italien). Quarzgefüge-Untersuchungen in Myloniten der Peio-Linie. Thesis, Univ Göttingen, 105 pp

Berger A, Rosenberg C, Schmid SM (1996) Ascent, emplacement and exhumation of the Bergell pluton within the Southern Steep Belt of the Central Alps. Schweiz Mineral Petrogr Mitteil 76:357-382

Berggren WA, Kent DV, Swisher CC III, Aubry MP (1995) A revised Cenozoic geochronology and chronostratigraphy. In: Berggren WA et al. (eds) Geochronology, time scales and global stratigraphic correlation. SEPM Spec Publ 54:129–212

Bigi G, Cosentino D, Parotto M, Sartori R, Scandone P (1990) Structural Model of Italy, sheets 1 and 2, CNR, Italy

Blanckenburg F von, Villa IM, Baur H, Morteani G, Steiger RH (1989) Time calibration of a PT-path from the western Tauern Window, Eastern Alps: the problem of closure temperatures. Contrib Mineral Petrol 101:1–11

Blanckenburg F von, Kagami H, Deutsch A, Wiedenbeck M, Oberli F, Meier M, Barth S, Fischer H (1998) The origin of Alpine plutons along the Periadriatic Lineament. Schweiz Mineral Petrogr Mitt 78:55–66

Bögel H (1975) Zur Literatur über die "Periadriatische Naht". Verh Geol Bundesanstalt Wien 1975:163–199

Borsi S, Del Moro A, Sassi FP, Zanferrari A, Zirpoli G (1978a) New geopetrologic and radiometric data on the Alpine history of the Austridic continental margin south of the Tauern window. Mem Sci Geol 32:1–17

Borsi S, Del Moro A, Sassi FP, Zirpoli G (1978b) On the age of the Vedrette di Ries (Rieserferner) massif and its geodynamic significance. Geol Rundsch 68:41–60

Bossart PJ, Meier M, Oberli F, Steiger RH (1986) Morphology versus U–Pb systematics in zircon: a high-resolution isotopic study of a zircon population from a Variscan dike in the Central Alps. Earth Planet Sci Lett 78:339–354

Castellarin A, Vai GB (1981) Importance of Hercynian tectonics within the framework of the Southern Alps. J Struct Geol 3:477–486

Cliff RA (1993) Isotopic dating of metamorphism and cooling. In: Funiciello R et al. (eds) Radiometric age determinations in orogenic processes: potentials and limits. Proc VI Summer School Earth Planetary Sciences, Siena, pp 131–140

Cumming GL, Richards JR (1975) Ore lead isotope ratios in a continuously changing earth. Earth Planet Sci Lett 28:155–171

Dal Piaz GV, Del Moro A, Martin S, Venturelli G (1988) Post-collisional magmatism in the Ortler-Cevedale Massif (northern Italy). Jahrb Geol Bundesanstalt Wien 131:533–551

Decker K, Peresson H (1996) Tertiary kinematics in the Alpine–Carpathian–Pannonian system: links between thrusting, transform faulting and crustal extension. In: Wessely G, Liebl W (eds) Oil and gas in Alpidic thrustbelts and basins of Central and Eastern Europe. EAGE Spec Publ 5:69–77

Del Moro A, Sassi F, Zirpoli G (1982) New radiometric data on the Alpine thermal history in the Ötztal-Merano area (Eastern Alps). Mem Sci Geol 35:319–325

Elias J (1998) The thermal history of the Ötztal-Stubai complex (Tyrol, Austria/Italy) in the light of the lateral extrusion model. Tübinger Geowiss Arb 42:1–172

Exner C (1976) Die geologische Position der Magmatite des periadriatischen Lineamentes. Verh Geol Bundesanstalt Wien 1976:3–64

Frank W, Hoinkes G, Purtscheller F, Thöni M (1987) The Austroalpine unit west of the Hohe Tauern: The Ötztal-Stubai complex as an example for the Eoalpine metamorphic evolution. In: Flügel HW, Faupl P (eds) Geodynamics of the Eastern Alps. Deuticke, Vienna, pp 179–225

Frisch W, Kuhlemann J, Dunkl I, Brügel A (1998) Palinspastic reconstruction and topographic evolution of the Eastern Alps during late Tertiary tectonic extrusion. Tectonophysics 297:1–15

Froitzheim N, Conti P, van Daalen M (1997) Late Cretaceous, synorogenic, low-angle normal faulting along the Schlinig fault (Switzerland, Italy, Austria) and its significance for the tectonics of the Eastern Alps. Tectonophysics 280:267–293

Fügenschuh B (1995) Thermal and kinematic history of the Brenner area (Eastern Alps, Tyrol). PhD thesis, ETH Zürich, 225 pp

Fügenschuh B, Seward D, Mancktelow N (1997) Exhumation in a convergent orogen: the western Tauern window. Terra Nova 9:213–217

Gansser A (1968) The Insubric Line, a major geotectonic problem. Schweiz Mineral Petrogr Mitt 48:123–143

Glutz C (1997) Kinematik der Jaufenlinie. Diploma thesis, ETH Zürich, 102 pp

Grasemann B, Mancktelow NS (1993) Two-dimensional thermal modelling of normal faulting: the Simplon Fault Zone, Central Alps, Switzerland. Tectonophysics 225:155–165

Gradstein FM, Agterberg FP, Ogg JG, Hardenbol J, van Veen P, Thierry J, Huang Z (1994) A Mesozoic time scale. J Geophys Res 99 B12:24051–24074

Grollimund B (1996) Tektonik südlich des westlichen Tauernfensters (Valsertal, Südtirol). Strukturgeologische Untersuchungen an der westlichen Fortsetzung der DAV und Interaktion mit oligozänen Gängen und Plutonen. Diploma thesis, ETH Zürich, 173 pp

Haas J, Kovacs S, Krystyn L, Lein R (1995) Significance of Late Permian–Triassic facies zones in terrane reconstructions in the Alpine–North Pannonian domain. Tectonophysics 242:19–40

Hennig S (1991) Der Insubrische Flysch im Gebiet von Bresimo bis Rumo. Diploma thesis, Univ Zürich, 87 pp

Heitzmann P (1987) Evidence of Late Oligocene/Early Miocene backthrusting in the Central Alpine "root zone". Geodin Acta 1:183–192

Hoinkes G, Kostner A, Thöni M (1991) Petrologic constraints for Eoalpine eclogite facies metamorphism in the Austroalpine Ötztal Basement. Mineral Petrol 43:237–254

Hurford AJ (1986) Cooling and uplift patterns in the Lepontine Alps (South Central Switzerland) and an age of vertical movement on the Insubric fault line. Contrib Mineral Petrol 92:413–427

Kleinschrodt R (1987) Quarzkorngefügeanalyse im Altkristallin südlich des westlichen Tauernfensters (Südtirol/Italien). Erlanger Geol Abh 114:1–82

Kretz R (1983) Symbols for rock-forming minerals. Am Mineral 68:277–279

Laubscher H (1970) Bewegung und Wärme in der alpinen Orogenese. Schweiz Mineral Petrogr Mitt 50:565–597

Laubscher H (1971) The large-scale kinematics of the Western Alps and the Northern Appenines and its palinspastic implications. Am J Sci 271:193–226

Laubscher HP (1988) Material balance in Alpine orogeny. Geol Soc Am Bull 100:1313–1328

Lo C-H, Lee JKW, Onstott TC (2000) Argon release mechanisms of biotite in vacuo and the role of short-circuit diffusion and recoil. Chem Geol 165:135–166

Maddock RH, Grocott J, van Nes M (1987) Vesicles, amygdales and similar structures in fault-generated pseudotachylytes. Lithos 20:419–432

Mancktelow NS (1992) Neogene lateral extension during convergence in the Central Alps: evidence from interrelated faulting and backfolding around the Simplonpass (Switzerland). Tectonophysics 215:295–317

Mancktelow NS, Stöckli DF, Grollimund B, Müller W, Fügenschuh B, Viola G, Seward D, Villa IM (this volume) The DAV and Periadriatic fault systems in the Eastern Alps south of the Tauern window. Int J Earth Sci DOI 10.1007/s005310000190 (this issue)

Martin S, Prosser G, Santini L (1991) Alpine deformation along the Periadriatic lineament in the Italian Eastern Alps. Ann Tect 5:118–140

Martin S, Prosser G, Morten L (1993) Tectono-magmatic evolution of sheeted plutonic bodies along the north Giudicarie line (northern Italy). Geol Rundsch 82:51–66

Meier R (1997) Kinematik der Mauls-Linie. Strukturgeologische Untersuchungen am SW-NE streichenden Segment der Periadriatischen Linie im Bereich des Penser Joch (Südtirol). Diploma thesis, ETH Zürich, 120 pp

Müller W (1998) Isotopic dating of deformation using microsampling techniques: the evolution of the Periadriatic Fault System (Alps). Ph.D. thesis, ETH Zürich, 135 pp

Müller W, Dallmeyer RD, Neubauer F, Thöni M (1999) Deformation-induced resetting of Rb/Sr and $^{40}Ar/^{39}Ar$ mineral systems in a low-grade, polymetamorphic terrane (Eastern Alps, Austria). J Geol Soc Lond 156:261–278

Müller W, Aerden D, Halliday AN (2000a) Isotopic dating of strain fringe increments: duration and rates of deformation in shear zones. Science 288:2195–2198

Müller W, Mancktelow NS, Meier M (2000b) Rb–Sr microchrons of synkinematic mica in mylonites. Earth Planet Sci Lett 180:385–397

Nemes F (1997) Kinematics of the Periadriatic Fault in the Eastern Alps. PhD thesis, Univ Salzburg, 220 pp

Neubauer F, Genser J (1990) Architektur und Kinematik der östlichen Zentralalpen – eine Übersicht. Mitt Naturwiss Vereins Steiermark 120:274–283

Neubauer F, Dallmeyer RD, Dunkl I, Schirnik D (1995) Late Cretaceous exhumation of the metamorphic Gleinalm dome, Eastern Alps: kinematics, cooling history and sedimentary response in a sinistral wrench corridor. Tectonophysics 242:79–98

Onstott TC, Miller ML, Ewing RC, Arnold GW, Walsh DS (1995) Recoil refinements: implications for the $^{40}Ar/^{39}Ar$ dating technique. Geochim Cosmochim Acta 59:1821–1834

Parolini F (1997) Kinematik der Jaufenlinie. Diploma thesis, ETH Zürich, 105 pp

Picotti V, Prosser G, Castellarin A (1995) Structures and kinematics of the Giudicarie–Val Trompia fold and thrust belt (Central Southern Alps, northern Italy). Mem Sci Geol 47:95–109

Prosser G (1998) Strike-slip movements and thrusting along a transpressive fault zone: the Giudicarie line (Insubric line, northern Italy). Tectonics 17:921–937

Prosser G (2000) The development of the North Giudicarie fault zone (Insubric line, northern Italy). J Geodyn 30:229–250

Pupin JP (1980) Zircon and granite petrology. Contrib Mineral Petrol 73:207–220

Ratschbacher L, Frisch W, Linzer HG, Merle O (1991) Lateral Extrusion in the Eastern Alps. Part 2: Structural analysis. Tectonics 10:257–271

Schäfer J (1989) Geologische Karte des unteren Kirchbergtales (Südtirol, Italien)–Kalium-Argon-Altersbestimmungen an Gesteinen der Peio-Linie und benachbarter Kristallineinheiten. Diploma thesis, Univ Göttingen, 64 pp

Schmid SM, Kissling E (2000) The arc of the western Alps in the light of geophysical data on deep crustal structure. Tectonics 19:62–85

Schmid SM, Aebli HR, Heller F, Zingg A (1989) The role of the Periadriatic Line in the tectonic evolution of the Alps. Geol Soc Am Spec Publ 45:153–171

Schmid SM, Pfiffner OA, Froitzheim N, Schönborn G, Kissling E (1996) Geophysical–geological transect and tectonic evolution of the Swiss-Italian Alps. Tectonics 15:1036–1064

Schmid SM, Pfiffner OA, Schönborn G, Froitzheim N, Kissling E (1997) Integrated cross section and tectonic evolution of the Alps along the Eastern Traverse. In: Pfiffner OA, Lehner P, Heitzmann P, Mueller S, Steck A (eds) Deep structure of the Swiss Alps. Birkhäuser, Basel, Switzerland, pp 289–304

Schulz B (1989) Jungalpidische Gefügeentwicklung entlang der Defereggen-Antholz-Vals-Linie (Osttirol, Österreich). Jahrb Geol Bundesanstalt Wien 132:775–789

Selverstone J (1988) Evidence for east–west crustal extension in the Eastern Alps: implications for the unroofing history of the Tauern Window. Tectonics 7:87–105

Spiess R (1995) The Passeier-Jaufen Line: a tectonic boundary between Variscan and eo-Alpine Meran-Mauls basement. Schweiz Mineral Petrogr Mitt 75:413–425

Sprenger WL (1996) Das Periadriatische Lineament südlich der Lienzer Dolomiten. Abh Geol Bundesanstalt Wien 52:1–220

Steiger RH, Jäger E (1977) Subcommision on geochronology: convention on the use of decay constants in geo- and cosmochronology. Earth Planet Sci Lett 36:359–362

Stöckli DF (1995) Tectonics SW of the Tauern Window (Mauls area, Südtirol). Southern continuation of the Brenner Fault Zone and its interaction with other large fault structures. Diploma thesis, ETH, Zürich, 270 pp

Suess E (1885) Das Antlitz der Erde, vol 1. Tempsky, Vienna

Thöni M (1981) Degree and evolution of the Alpine metamorphism in the Austroalpine unit W of the Hohe Tauern in the light of K/Ar and Rb/Sr age determinations on micas. Jahrb Geol Bundesanstalt Wien 124:111–174

Thöni M (1988) Rb–Sr isotopic resetting in mylonites and pseudotachylites: implications for the detachment and thrusting of the Austroalpine Basement Nappes in the Eastern Alps. Jahrb Geol Bundesanstalt Wien 131:169–201

Thöni M (1999) A review of geochronological data from the Eastern Alps. Schweiz Mineral Petrogr Mitt 79:209–230

Tollmann A (1978) Die Seitenverschiebung an der Periadriatischen Naht auf Grund des Vergleiches der Triasfazies. Österr Akad Wiss Schriftenreihe Erdwiss Komm 4:179–192

Turner G, Wang SS (1992) Excess Argon, crustal fluids and apparent isochrons from crushing K-feldspar. Earth Planet Sci Lett 110:193–211

Villa IM (1983) $^{40}Ar/^{39}Ar$ chronology of the Adamello gabbros, Southern Alps. Mem Soc Geol Ital 26:309–318

Viola G (2000) Kinematics and timing of the Periadriatic fault system in the Giudicarie region (central–eastern Alps). PhD thesis, ETH Zürich, 205 pp

Wagreich M, Faupl P (1994) Paleogeography and geodynamic evolution of the Gosau Group of the Northern Calcareous Alps (Late Cretaceous, Eastern Alps, Austria). Palaeogeogr Palaeoclimatol Palaeoecol 110:235–254

Weissert HJ, Bernoulli D (1985) A transform margin in the Mesozoic Tethys: evidence from the Swiss Alps. Geol Rundsch 74:665–679

Werling E (1992) Tonale-, Pejo- und Judicarien-Linie: Kinematik, Mikrostrukturen und Metamorphose von Tektoniten aus räumlich interferierenden aber verschiedenaltrigen Verwerfungszonen. PhD thesis, ETH Zürich, 276 pp

Wiedenbeck M (1986) Structural and isotopic age profile across the Insubric Linie, Mello, Valtellina, N. Italy. Schweiz Mineral Petrogr Mitt 66:211–227

Wiedenbeck M, Allé P, Corfu F, Griffin WL, Meier M, Oberli F, Quadt A von, Roddick JC, Spiegel W (1995) Three natural zircon standards for U–Th-Pb, Lu–Hf, trace element and REE analyses. Geostandards Newslett 19:1–23

Zarske G (1989) Gefügekundliche und kristallingeologische Untersuchungen zur alpinen Störungskinematik im Umbiegungsbereich von Tonale- und Judicarien-Linie. Gött Arb Geol Paläontol 38:1–142